A marker-point-based model for simulation of elastic surface deformation

by
Kamryn Spinelli

Advisor: Professor Min Wu

11 December 2020

A Major Qualifying Project submitted to the Faculty of Worcester Polytechnic Institute in partial fulfillment of the requirements for the degree of Bachelor of Science in Mathematical Sciences

Abstract

In differential geometry, surfaces of revolution form a large class of illuminating examples. These surfaces are also useful in applications, where the assumption of rotational symmetry can simplify a modeling problem substantially. Particularly for some problems in biology, one might want to simulate the deformation of such surfaces. One discretized model based on interpolation by linear segments has been presented previously in [Che+20]. We present a new model based on interpolation by arcs of parabolas in a way that properly generalizes the previous approach; a third model which is useful as a benchmark is obtained as a special case. We present the results of the simulation and discuss the models' performance and error properties.

Acknowledgments

I would like to thank Professor Min Wu for her invaluable guidance over the course of this project. I would also like to thank all of my professors at WPI. They made me a better student and mathematician.

Contents

1 Introduction

Among smooth surfaces embedded in $\mathbb{R}^3$, surfaces of revolution are some of the easiest to characterize and provide a large selection of examples for various geometric properties. In addition to their uses in abstract differential geometry, however, surfaces of revolution find wide usage in applications. One such example is in mathematical biology, where surfaces of revolution can be used as models for thin membranes on the cellular level. In the case of plant or other walled cells, the structure of the cell outline is dominated by the mechanics of the cell wall and the internal turgor pressure, so a simplified model of the cell outline based on a surface of revolution is suitable. For animal cells, however, the cellular structure results primarily from

the internal cytoskeleton and therefore such a model is not suitable for accurately describing the structure of the cell.

Another wonderful application of thin-surface modeling is to cell nucleus force sensing. It has been shown [EA+17] that exerting force on cell nuclei causes nuclear pore complexes to open, encouraging transport across the nuclear membrane. However, it is not known whether the force sensing scheme is more dependent on tension or curvature; one could simulate the nuclear deformation under external force and use empirical data from the lab to infer the sensitivity of nuclear transport to each of these factors.

The mechanics – namely tensions and pressures – of surfaces of revolution are generally well-understood in the theoretical sense but an accurate, high-performance computer simulation is difficult to achieve. It is natural to take advantage of the symmetry of such axiosymmetric surfaces and translate questions about the surface embedded in three-dimensional space to questions about its generating curve embedded in two dimensions. With high-resolution small-scale imaging one can see membrane outlines which are thought of as the generating curves of the membrane surface, then choose a set of marker points living on this generating curve, and hence approximate the geometry of the surface. In this setup, the process of reconstructing the geometry from this set of marker points is highly dependent on how one interpolates the generating curve between consecutive marker points. In this document we review a model based on interpolation by linear segments and we construct a new higher-order model based on interpolation by arcs of parabolas. The parabolic arcs model degenerates into linear segments as a special case, yielding a third model which retains the geometry of the linear model but the force computation of the parabolic model. In all three of these models, the surface geometry is reconstructed from a set of marker points on the membrane outline and the resultant force is defined in terms of this geometry. Furthermore, we show evidence to suggest that the new parabolic arcs model suitably generalizes the linear model.

The model based on parabolic arcs is not the only way to generalize the standard linear segments approach. We refer the reader to [Poz92] for a discussion of another higher-order scheme based on interpolation by circular arcs and a sketch of an interpolation method based on cubic splines. Also important to note is the fact that our model relies heavily on the symmetry of axiosymmetric surfaces. For a full three-dimensional model, the situation is significantly more complicated. We refer the reader to [Xu+18] for an example of how one might reconstruct three-dimensional geometry from general point cloud data.

As a final note, there is also interest in modelling the growth of walled cells. At the current time, the models we present do not allow for growth or atrophy, i.e. the amount of membrane material is presumed to be constant, but the models can be extended to simulate this phenomenon as well.

2 Background

While our models are essentially agnostic in their application, we will frequently remember the biological analogy and think of the surface of revolution as a membrane on the cellular level, for example, the cell wall in a plant or fungal cell. In this case we assume the internal mechanics of the cell due to its cytoskeleton to be negligible and focus only on the elastic mechanics of the cell boundary instead.

The problem of simulating such an axiosymmetric membrane in this way has been approached before in the literature. However, the question of tip behavior for the surface of revolution is delicate. It is natural to use polar coordinates to parametrize the surface of revolution, and map the origin to the tip, curves of constant r to the circumferences, and curves of constant θ to the meridians of the surface. But in polar coordinates, the origin is a singular point in the sense that many coordinate curves converge there. Because of this, the material quantities such as strain must be isotropic at the tip (viz. at the origin in the polar coordinate system) in order to make physical sense. And in order to define a force at the tip, either the tip must be smooth or some boundary condition must be imposed there, because otherwise force computation may not be well-defined. Earlier works deal with the question of tip behavior in a variety of ways; two of the most compelling models are due to Yanagisawa et al., and Goriely and Tabor.

In [Yan+15], Yanagisawa et al. use the FEM software Abaqus and designate an isotropic zone near the tip. This is geometrically and mechanically sensible at the tip point for the reasons described above. However, this approach causes numerical problems at the interface between the tip isotropic zone and the

rest of the membrane; it is apparent from Figures 2j and 2k of that article that the tensions are not smooth over the surface, contradicting Laplace's Law (Equation 2).

[GT03b] models growth at the tip of a walled cell where the growth is observed to be self-similar, in other words preserving the tip geometry as the cell grows. To do this, the authors assume the growth to be pressure-driven and define an effective pressure quantity given as a ratio of turgor pressure and local elastic modulus. By setting up a system of coupled ODEs in the geometric quantities $r(s(\sigma))$ and $\alpha(s(\sigma))$ of the generating curve with prescribed distributions of mechanical parameters along the profile curve, one can solve for the cell outline. Reparametrizing the arclength to be the new material coordinate and iterating allows one to simulate deformation over time. While this does produce compelling results, one can show that the coupled ODE system that Goriely and Tabor give violates the Lipschitz condition at the tip point, so the Picard-Lindelöf theorem cannot be applied and the problem might not even be well-posed in the first place.

In this paper we will focus on a discretized vertex model based on interpolation by parabolic arcs which generalizes the ideas in a previous model based on interpolation by linear segments [Che+20]. In that system, linear segments cannot ensure smoothness of the approximated surface outline at the tip, so a boundary condition is imposed for that point (see Section 3.2).

By switching to a higher-order discretization and interpolation system, we hope to achieve better accuracy and convergence in the simulation compared to our previous approach based on linear segments. This does not change the fact that the tip must be treated specially, remembering that the surface is assumed rotationally symmetric. For the linear segments model, we must specify the force balance equation for the tip point. In our parabolic arcs model, we compute the force on the tip point exactly as it is computed for the other points, but the construction of tip-adjacent patches is different from the others – in other words, we don't specify the tip force but instead we specify the tip geometry. It is clear that no matter the model used, the tip requires special treatment.

3 Models

3.1 The overarching force-balance equation

In this section we describe three models for the mechanics of axiosymmetric surfaces. Each model is based on the local force-balance equation given in terms of the surface's generating curve:

$$\underbrace{\frac{d(\sigma_s \hat{t})}{ds}}_{(1)} + \underbrace{\frac{\sigma_s - \sigma_\theta}{r(s)}\hat{r}}_{(2)} - \underbrace{\frac{\sigma_s \sin\alpha(s)}{r(s)}\hat{n}(s)}_{(3)} + \underbrace{P\hat{n}(s)}_{(4)} = 0. \tag{1}$$

This force-balance equation has been used in other articles, for example [Che+20]. Here,

- σ_s and σ_θ are tensions on the surface in the meridional and circumferential directions respectively,
- $r(s)$ is the r-coordinate of the point on the generating curve,
- $\hat{t}(s)$ is the unit tangent vector pointing in the direction of increasing arclength,
- $\hat{n}(s)$ is the outward unit normal vector to the generating curve,
- $\hat{r}$ is the unit basis vector pointing in the positive r-direction,
- $\alpha(s)$ is the signed angle between $\hat{t}(s)$ and $\hat{r}$ at the point $(z(s), r(s))$ on the curve,
- P is turgor pressure, a constant.

This expression is obtained by computing the surface divergence of the Cauchy stress tensor, plus a pressure term:

$$\nabla_s \cdot \sigma + P\hat{n}, \quad \text{where} \quad \nabla_s = \hat{t}\frac{\partial}{\partial s} + \frac{\hat{\theta}}{r}\frac{\partial}{\partial \theta} \quad \text{and} \quad \sigma = \sigma_s \hat{t} \otimes \hat{t} + \sigma_\theta \hat{\theta} \otimes \hat{\theta}.$$

There is a particularly nice interpretation of the force in terms of the curve's moving Frenet frame. Along the $\hat{n}$-direction, it expresses Laplace's Law

$$\kappa_s \sigma_s + \kappa_\theta \sigma_\theta = P. \tag{2}$$

Along $\hat{t}$, it gives the relation

$$\kappa_\theta \sigma_s = P/2. \tag{3}$$

In the discretized system, each of our models compute the force on the i-th marker point by integrating the left-hand side of Equation 1 in a neighborhood corresponding to the arclength interval $[s^{i-1/2}, s^{i+1/2}]$. The details of this integration depend on the model in question. The difference between the three models is the geometry of the patches between points. The most simple approach models the patches as linear segments, while a more sophisticated version models the patches as arcs of parabolas. This differing geometry affects the computed force on each marker point when we integrate the left-hand side of Equation 1. Our third approach uses the force computation from the parabolic arcs model but forces each parabola to degenerate into a line segment.

Note that it is vital for the profile curve to be smooth at the tip in order to ensure that quantity (3) doesn't have a singularity there. Quantity (2) may still have a singularity at the tip, but it is odd about the tip point, so one may discard it when computing the tip force.

3.1.1 Tension computation

In order to make mechanical sense of the interpolated surface in each of the three models, we must first decide how to measure the material strains. We will approximate the local meridional strain $\lambda_s = ds/ds^0$ by $\frac{l}{l_0}$ where l is the current arclength of the patch and l_0 is its intrinsic arclength; these arclengths should be computed according to whatever geometry is assumed by the model between marker points. We also approximate the meridional strain λ_θ by r/r_0 where r is the current $\hat{r}$-coordinate of the midpoint of the patch, and r_0 is the intrinsic $\hat{r}$-coordinate of the midpoint of the patch. It would be more accurate to instead define r to be the average $\hat{r}$-coordinate over the patch (and similarly for r_0), but the midpoint-based computation will likely be a sufficient approximation.

Each model assumes that σ_s and σ_θ, which are the tensions in the meridional and circumferential directions respectively, are constant on each patch. With the strain computation in hand, we define these tensions on each patch as nonlinear functions of the strains:

$$\begin{cases} \sigma_s = \frac{1}{2}\mu_h \left(\left(\frac{1}{\lambda_\theta}\right)^2 - \left(\frac{1}{\lambda_s}\right)^2 \right) + K_h \left(\lambda_s \lambda_\theta - 1\right), \\ \sigma_\theta = \frac{1}{2}\mu_h \left(\left(\frac{1}{\lambda_s}\right)^2 - \left(\frac{1}{\lambda_\theta}\right)^2 \right) + K_h \left(\lambda_s \lambda_\theta - 1\right). \end{cases} \tag{4}$$

This is the Evans law [Dim12]. Since we are modeling the membrane as a thin surface, a two-dimensional tension law such as the Evans law is suitable. If the membrane thickness were non-negligible, a more sophisticated approach such as a neo-Hookean model would be necessary.

The use of nonlinear elastic stress-strain laws is somewhat common for cellular-level biological applications (for examples, see [WBA15; GTT09; GT03a; GT03b]), and the choice of which law to use is not of great importance. The difference between the various laws deals mostly with how the area dilation and shear deformations are combined to produce the overall tensions [Dim12]. As long as a sensible tension law is used, we are confident our models will be compatible.

3.1.2 A remark on notation

Throughout this section we need to consider quantities defined at a marker point or on patches in the discretized system. To index these quantities, we use the following convention. Quantities defined at the i-th marker point receive a subscript i, such as t_i. Quantities defined on the patch immediately preceding the i-th marker point receive a superscript $i-1/2$, as in $\sigma_s^{i-1/2}$. Similarly, a superscript $i+1/2$ indicates that the quantity is defined on the patch immediately following the i-th marker point.

With this convention, given a (piecewise smooth) parametrization for a part of the profile curve, we will use s_i and t_i to denote the arclength and time, respectively, corresponding to the i-th marker point. Similarly, $s^{i-1/2}$ and $t^{i-1/2}$ denote the arclength and time, respectively, at the midpoint of the patch preceding the i-th marker point. (We define the midpoint as the point dividing the patch into two equal arclengths.) A similar meaning is given to $s^{i+1/2}$ and $t^{i+1/2}$.

3.2 The linear segments model

In the linear segments model, the patch between adjacent marker points is taken to be the line segment connecting them. This is perhaps the most simple model possible and it has been utilized before, for example in [Che+20]. Because of the simplicity of this model, r is an affine function of z, and $\alpha(s)$ is constant on each patch, so integrating Equation 1 over the neighborhood $[s^{i-1/2}, s^{i+1/2}]$ of the i-th marker point is especially easy. This gives the approximate force-balance equation

$$\begin{aligned}
&(\sigma_s\hat{t})^{i+1/2} - (\sigma_s\hat{t})^{i-1/2} \\
&\quad + \ln\left(\frac{r(s_i)}{r(s^{i-1/2})}\right)\left(\frac{(\sigma_s-\sigma_\theta)\hat{r} - (\sigma_s\sin\alpha)\hat{n})}{\cos\alpha}\right)^{i-1/2} \\
&\quad + \ln\left(\frac{r(s^{i+1/2})}{r(s_i)}\right)\left(\frac{(\sigma_s-\sigma_\theta)\hat{r} - (\sigma_s\sin\alpha)\hat{n})}{\cos\alpha}\right)^{i+1/2} \\
&\quad + \frac{P}{2}((s_i - s^{i-1/2})\hat{n}^{i-1/2} + (s^{i+1/2} - s_i)\hat{n}^{i+1/2}) = 0
\end{aligned} \tag{5}$$

for the non-tip points. For the tip point, which has index $N+1$, we have $r = 0$ and thus Equation 5 does not make sense. Therefore, at the tip, we implement Equation 3 and hence impose the force boundary condition

$$\left\langle -(\sigma_s\sin\alpha)^{N+1/2} + \frac{Pr(s^{N+1/2})}{2}, 0\right\rangle = \langle 0, 0\rangle\,. \tag{6}$$

3.3 The parabolic arcs model

Motivated by the unexciting performance of the linear segments model (overall roughly linear order of accuracy; see Sections 4, 5, 6), we wish to devise a new model which generalizes and improves upon the previous model. The most obvious way to improve is by changing the way we interpolate between marker points. With this in mind, the parabolic arcs model interpolates between consecutive marker points using an arc of a parabola. Because three points are needed to uniquely define a parabola, there is no canonical way to construct this parabola, but we base our method on the following observation. Suppose that the two marker points p_1 and p_2 bordering the patch lie on a horizontal line. We can construct a parabola passing through q_1, the marker point preceding p_1, and a parabola passing through q_2, the marker point following p_2. Each of these parabolas is of the form $\frac{(x-a)}{\lambda^2} + b$; let λ_1 be the λ associated with the fitting of the point q_1 and similarly for λ_2. The quantities $1/\lambda_1$, $1/\lambda_2$ are closely related to the curvature properties of the parabolas. Thus, finding the "average geometry" of the two fittings corresponds to taking $1/\lambda$ as the arithmetic mean of $1/\lambda_1$ and $1/\lambda_2$. This notion is explained further in the following discussion.

3.3.1 Geometric preliminaries

In constructing the parabolic patches, we consider general parabolas in the plane (without restriction on orientation with respect to standard coordinates). There are four parameters characterizing such a parabola:

- Stretch factor λ: This parameter describes how stretched the parabola is along the direction orthogonal to its axis of symmetry. For generality, we define $\lambda \in \widehat{\mathbb{R}}$, the projectively extended reals, i.e. the set $\mathbb{R}$ together with the single extra element ∞ which neighbors both 'ends' of the real line. By convention we set $\frac{1}{\infty} = 0$, $\frac{1}{0} = \infty$. If the parabola is written in the form $r = f(z)$ with vertex at the origin (up to a rigid motion in the plane), then λ stretches the parabola horizontally: $r = \frac{z^2}{\operatorname{sgn}(\lambda)\lambda^2}$. The factor of $\operatorname{sgn}(\lambda)$ causes the parabola to open up or down depending on the sign (incorporating the signed curvature rather than unsigned curvature). However, setting $\lambda = 0$ is problematic even inside $\widehat{R}$, because it means that $f(z) = \infty$ almost everywhere. We disregard this case here and in the following discussion.

- Rotation angle θ: This parameter describes the angle by which one must rotate counterclockwise a parabola of the form $r = f(z)$ in order to obtain the desired parabola.

- z and r translations T_z and T_r: These parameters are the coordinates of the vertex of the parabola; if we translate a parabola of the form $r = f(z)$ whose vertex is the origin by (T_z, T_r), we obtain a parabola whose vertex is the desired point.

The parametric expression for such a parabola can be written as follows:

$$f(t) = (z(t), r(t)) = \begin{pmatrix} \cos\theta & -\sin\theta \\ \sin\theta & \cos\theta \end{pmatrix} \begin{pmatrix} t \\ -\frac{t^2}{\operatorname{sgn}(\lambda)\lambda^2} \end{pmatrix} + \begin{pmatrix} T_z \\ T_r \end{pmatrix} = \begin{pmatrix} t\cos\theta - \frac{-t^2}{\operatorname{sgn}(\lambda)\lambda^2}\sin\theta + T_z \\ t\sin\theta + \frac{-t^2}{\operatorname{sgn}(\lambda)\lambda^2}\cos\theta + T_r \end{pmatrix}. \tag{7}$$

3.3.2 Construction of the parabola in a rotated coordinate system

We will determine the parameters $\lambda, \theta, T_z, T_r$ as illustrated in Figure 1. Construct the perpedicular bisector of the line segment p_1p_2 and label the midpoint of p_1p_2 as b. Let ℓ be the length of the segment p_1b. Transform the plane by a rigid motion such that b is the origin, p_1p_2 lies in the x-axis, p_1 has coordinates $(-\ell, 0)$, and p_2 has coordinates $(\ell, 0)$. From here we must assume that q_1, p_1, p_2, q_2 are arranged in order horizontally in the rotated coordinate system; this can be guaranteed with a fine enough discretization. Our patch between marker points will come from a parabola of the form $f(x) = V - \frac{x^2}{\operatorname{sgn}(\lambda)\lambda^2}$ which passes through p_1 and p_2. In order for this to be the case, we must have $V = \frac{\ell^2}{\operatorname{sgn}(\lambda)\lambda^2}$. By varying the parameter λ, we obtain a 1-dimensional family of parabolas which pass through p_1 and p_2.[1] The degenerate case occurs when $\lambda \to \infty$, in which case the parabola becomes a line passing through p_1 and p_2 (see Section 3.4).

[1] We could have chosen to instead express λ in terms of V and control V as a parameter. Why didn't we do so? This is because λ has a stronger geometric meaning as the stretching factor of the parabola. Indeed, the curvature of the parabola at its vertex is $-2/\lambda^2$.

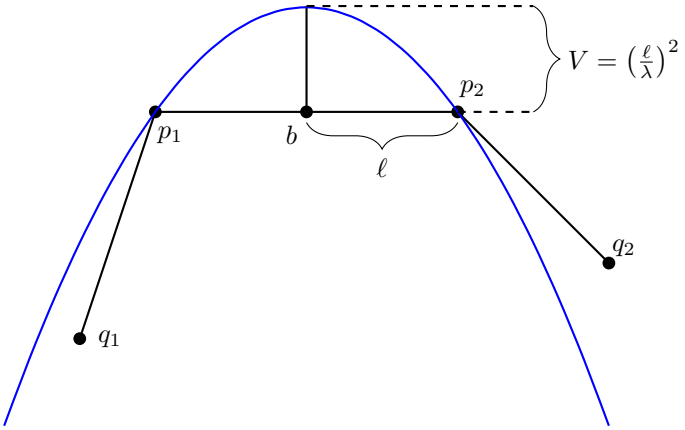

Figure 1: Fitting the parabolic arc to the points p_1, p_2, q_1, q_2 in the rotated coordinate system. The points and connecting segments are shown in black and a candidate approximating parabola is shown in blue.

Our construction compromises between exactly fitting the point q_1 and exactly fitting the point q_2. To do this, we compute the λ_1, λ_2 which fit the curve $f(t)$ to the points q_1, q_2 respectively. (Such λ_1, λ_2 are unique as a consequence of the fact that three points determine a parabola.) To compute these, let x_1, y_1 be the coordinates of q_1 in this rotated coordinate system. Then we have

$$\begin{aligned} y_1 &= V - \frac{x_1^2}{\lambda_1^2} \\ y_1 &= \frac{\ell^2 - x_1^2}{\lambda_1^2} \\ \lambda_1^2 &= \frac{\ell^2 - x_1^2}{y_1} \\ \lambda_1 &= \sqrt{\frac{\ell^2 - x_1^2}{y_1}}, \end{aligned}$$

where for negative a, we set $\sqrt{a} = -\sqrt{|a|}$. Similarly, we compute $\lambda_2 = \sqrt{\frac{\ell^2 - x_2^2}{y_2}}$ to fit q_2. We then set λ to be the harmonic mean of λ_1 and λ_2, that is,

$$\lambda = \frac{2\lambda_1\lambda_2}{\lambda_1 + \lambda_2}. \tag{8}$$

We choose to use the harmonic mean rather than the arithmetic mean because this acts as a sort of "average" of the geometries of the two curves associated with λ_1 and λ_2; alternatively, one could say that $\frac{1}{\lambda}$ more naturally measures the geometry of the curve. For example, as λ approaches ∞, the parabola degenerates into a line; this is the 'average behavior' when q_1 and q_2 are rotationally symmetric with respect to b (that is, when b is the midpoint of q_1q_2).

Recall that we disregarded the case $\lambda = 0$ earlier. Clearly, from Equation 8, $\lambda = 0$ iff $\lambda_1 = 0$ or $\lambda_2 = 0$; in order for this to be the case, two of the three points (p_1 and p_2, and one of q_1 and q_2) would need to have equal x-coordinates in this rotated coordinate system. This is the only scenario in which there is no unique parabola passing through three points. Indeed, in this case there is no sensible way to define an interpolating parabola because the parabola would need to have infinite derivative between two of the points; this is not possible for any polynomial.

Overall, we set

$$f(x) = \frac{1}{\operatorname{sgn}(\lambda)\lambda^2}(\ell^2 - x^2), \tag{9}$$

where $\operatorname{sgn}(\lambda)$ is the sign function, equal to 0 if $\lambda = 0$ and $\lambda/|\lambda|$ otherwise. The purpose of the $\operatorname{sgn}(\lambda)$ in the denominator is to ensure that if both q_1 and q_2 are on the same side of the line p_1p_2, then the parabola opens toward those points rather than away from them.

If $\lambda_1 = -\lambda_2$, Equation 8 gives $\lambda = \infty$ because λ is considered to be in the projectively extended reals. Geometrically, in this case, the signed curvatures associated with fitting either q_1 or q_2 are equally opposite. Thus the 'curvature average' of fitting q_1 or q_2 would be zero; that is, the interpolating arc is just a linear segment.

3.3.3 Translating back to the original (z, r) coordinate system

From here we want to translate back to the parameters $\lambda, \theta, T_z, T_r$ originally described. λ remains the same; as a geometric quantity it has no dependence on the coordinates chosen, so it is the same in the rotated coordinate system and the original (z, r) coordinate system. For the other parameters we refer to Figure 2. We denote by β the signed angle formed by rotating counterclockwise from the coordinate vector $\hat{z}$ to the outward-facing normal of the linear segment p_1p_2. We also denote by α the signed angle from $\hat{t}$ to $\hat{r}$, as in [Che+20]. The relationship between α and β is $\beta = \pi - \alpha$.

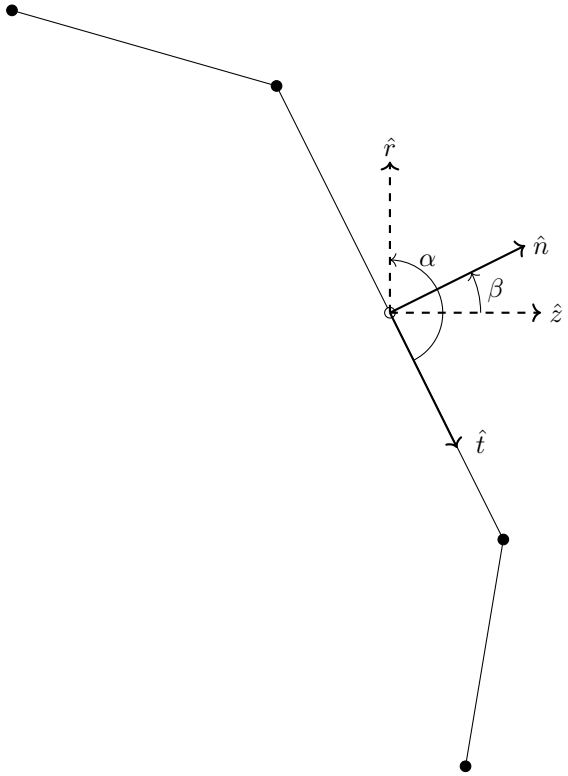

Figure 2: Tangent and normal vectors to the linear segments between marker points in the original (z, r) coordinate system.

The vertex of the parabola in (z, r) coordinates is

$$(T_z, T_r) = b + V(\cos\beta, \sin\beta) = b + \frac{\ell^2}{\operatorname{sgn}(\lambda)\lambda^2}(\cos\beta, \sin\beta). \tag{10}$$

For the parameter θ, notice that in the rotated coordinate system, the normal vector of the segment p_1p_2 points upward. Thus we find that $\theta = \beta - \frac{\pi}{2}$, and so $\sin\theta = \sin(\beta - \frac{\pi}{2}) = -\cos\beta$ and $\cos\theta = \cos(\beta - \frac{\pi}{2}) =$

$\sin\beta$. To mimic the notation used in other articles ([Che+20]), note that since $\beta = \pi - \alpha$, $\sin\beta = \sin(\pi-\alpha) = \sin\alpha$ and $\cos\beta = \cos(\pi-\alpha) = -\cos\alpha$. We also denote the components of b in the (z,r) coordinate system by by (b_z, b_r). Using Equation 7, the expression of the parabola in (z,r) coordinates is

$$f(t) = \begin{pmatrix} t\cos\theta - \frac{-t^2}{\mathrm{sgn}(\lambda)\lambda^2}\sin\theta + T_z \\ t\sin\theta + \frac{-t^2}{\mathrm{sgn}(\lambda)\lambda^2}\cos\theta + T_r \end{pmatrix} = \begin{pmatrix} t\sin\beta + \frac{-t^2+\ell^2}{\mathrm{sgn}(\lambda)\lambda^2}\cos\beta + b_z \\ -t\cos\beta + \frac{-t^2+\ell^2}{\mathrm{sgn}(\lambda)\lambda^2}\sin\beta + b_r \end{pmatrix} = \begin{pmatrix} t\sin\alpha - \frac{-t^2+\ell^2}{\mathrm{sgn}(\lambda)\lambda^2}\cos\alpha + b_z \\ t\cos\alpha + \frac{-t^2+\ell^2}{\mathrm{sgn}(\lambda)\lambda^2}\sin\alpha + b_r \end{pmatrix}. \tag{11}$$

From now on we will prefer the expression in terms of α to match the literature.

3.3.4 Special treatment at the tip

For the force-balance equation (Equation 1) to be well-defined at the tip, the tip of the surface must be smooth. However, if we construct the patches neighboring the tip point in the way described above, this assumption may be violated because there is no guarantee that the outward unit normal approaches the basis vector $\hat{z}$ as $r(s) \to 0$. In order to address this issue, we construct the parabola passing through the tip marker point p and the preceding and following marker points q_1 and q_2. This is equivalent to setting $\alpha = \pi$, $\ell = (q_1)_r$, $b = \frac{q_1+q_2}{2}$, and $\lambda = \frac{(q_1)_r}{\sqrt{p_z-(q_1)_z}}$ in Equation 11, and it produces a parabola which opens along the $\hat{z}$-axis. Then we take the upper and lower halves of this parabola, respectively, to be the upper and lower patches neighboring the tip point. It is clear to see that $\hat{n} \to \hat{z}$ as $r(s) \to 0$ because this is the vertex of the parabola; therefore the tip smoothness condition is satisfied.

3.3.5 Force computation in the parabolic arcs model

In order to integrate Equation 1 in the neighborhood of a marker point, we need to know the arclength element ds of each patch. For the parabolic arcs, we could compute ds in (r,z) coordinates but it is easier to compute it in the rotated coordinate system of Section 3.3.2. In the rotated coordinates, $f(t) = V - \frac{t^2}{\mathrm{sgn}(\lambda)\lambda^2}$ and $f'(t) = -\frac{2t}{\mathrm{sgn}(\lambda)\lambda^2}$. Thus, at the point $f(t)$ on the parabola,

$$ds = \sqrt{1+f'(t)^2}dt = \sqrt{1+\frac{4t^2}{\lambda^4}}\,dt. \tag{12}$$

We note that while the tensions σ_s, σ_θ are assumed constant on each patch, the quantities $\alpha(s), r(s), \hat{t}(s), \hat{n}(s)$ are more complicated than in the linear segments model and must be derived from Equation 11. By integrating Equation 1 between $s^{i-1/2}$ and $s^{i+1/2}$, we find that the force on the i-th marker point is

$$S_1 + S_2 + S_3 + S_4, \tag{13}$$

where

$$S_1 = \int_{s^{i-1/2}}^{s^{i+1/2}} \frac{d(\sigma_s\hat{t})}{ds}\,ds = \left[\sigma_s\hat{t}(s)\right]_{s=s^{i-1/2}}^{s^{i+1/2}} = (\sigma_s\hat{t}(s^{i+1/2}))^{i+1/2} - (\sigma_s\hat{t}(s^{i-1/2}))^{i-1/2}, \tag{14}$$

$$\begin{aligned} S_2 &= \int_{s^{i-1/2}}^{s^{i+1/2}} \frac{\sigma_s-\sigma_\theta}{r(s)}\hat{r}\,ds = \int_{s^{i-1/2}}^{s_i} \frac{(\sigma_s-\sigma_\theta)^{i-1/2}}{r^{i-1/2}(s)}\hat{r}\,ds + \int_{s_i}^{s^{i+1/2}} \frac{(\sigma_s-\sigma_\theta)^{i+1/2}}{r^{i+1/2}(s)}\hat{r}\,ds \\ &= \int_{t^{i-1/2}}^{t_i} \frac{(\sigma_s-\sigma_\theta)^{i-1/2}\hat{r}}{t\cos(\alpha^{i-1/2}) + \frac{-t^2+(\ell^{i-1/2})^2}{(\mathrm{sgn}(\lambda)\lambda^2)^{i-1/2}}\sin(\alpha^{i-1/2}) + b_r^{i-1/2}}\sqrt{1+\frac{4t^2}{(\lambda^{i-1/2})^4}}\,dt \\ &\quad + \int_{t_i}^{t^{i+1/2}} \frac{(\sigma_s-\sigma_\theta)^{i+1/2}\hat{r}}{t\cos(\alpha^{i+1/2}) + \frac{-t^2+(\ell^{i+1/2})^2}{(\mathrm{sgn}(\lambda)\lambda^2)^{i+1/2}}\sin(\alpha^{i+1/2}) + b_r^{i+1/2}}\sqrt{1+\frac{4t^2}{(\lambda^{i+1/2})^4}}\,dt, \end{aligned} \tag{15}$$

$$
\begin{aligned}
S_3 &= \int_{s^{i-1/2}}^{s^{i+1/2}} \frac{-\sigma_s \sin\alpha(s)}{r(s)} \hat{n}\ ds \qquad (16)\\
&= \int_{s^{i-1/2}}^{s_i} \frac{-(\sigma_s)^{i-1/2}\sin(\alpha^{i-1/2}(s))}{r^{i-1/2}(s)} \hat{n}^{i-1/2}(s)\ ds + \int_{s^{i-1/2}}^{s_i} \frac{-(\sigma_s)^{i+1/2}\sin(\alpha^{i+1/2}(s))}{r^{i+1/2}(s)} \hat{n}^{i+1/2}(s)\ ds \\
&= \int_{t^{i-1/2}}^{t_i} \frac{-(\sigma_s)^{i-1/2}\left(\sin(\alpha^{i-1/2}) + \frac{2t\cos(\alpha^{i-1/2})}{(\mathrm{sgn}(\lambda)\lambda^2)^{i-1/2}}\right)}{t\cos(\alpha^{i-1/2}) + \frac{-t^2+(\ell^{i-1/2})^2}{(\mathrm{sgn}(\lambda)\lambda^2)^{i-1/2}}\sin(\alpha^{i-1/2}) + b_r^{i-1/2}} \hat{n}^{i-1/2}(t)\ dt \\
&\quad + \int_{t_i}^{t^{i+1/2}} \frac{-(\sigma_s)^{i+1/2}\left(\sin(\alpha^{i+1/2}) + \frac{2t\cos(\alpha^{i+1/2})}{(\mathrm{sgn}(\lambda)\lambda^2)^{i+1/2}}\right)}{t\cos(\alpha^{i+1/2}) + \frac{-t^2+(\ell^{i+1/2})^2}{(\mathrm{sgn}(\lambda)\lambda^2)^{i+1/2}}\sin(\alpha^{i+1/2}) + b_r^{i+1/2}} \hat{n}^{i+1/2}(t)\ dt,
\end{aligned}
$$

$$
S_4 = \int_{s^{i-1/2}}^{s^{i+1/2}} P\hat{n}\ ds = P\int_{t^{i-1/2}}^{t_i} \hat{n}^{i-1/2}(t)\sqrt{1+\frac{4t^2}{(\lambda^{i-1/2})^4}}\ dt + P\int_{t_i}^{t^{i+1/2}} \hat{n}^{i+1/2}(t)\sqrt{1+\frac{4t^2}{(\lambda^{i+1/2})^4}}\ dt. \quad (17)
$$

3.4 The degenerate parabolic arcs model

This model is mostly identical to the parabolic arcs model, except on each patch we set $\lambda = \infty$. Recalling that $1/\lambda$ is related to the curvature of the parabola, we observe that this causes the parabola to degenerate into a line segment. Furthermore, the integrals in Equations 14, 15, 16, 17 simplify and thus recover the force balance equation from Section 3.2. This is encouraging evidence to suggest that the parabolic arcs model properly generalizes the linear segments model. However, for the degenerate parabolic arcs model we will compute the marker point force by numerically integrating Equations 14, 15, 16, 17 with $\lambda = \infty$.

Because the degenerate parabolic arcs model retains error due to the inaccurate geometry of the linear segments model and also error due to numerical integration, we expect it to perform worse than either of the other two models. This model is not tremendously useful for practical purposes, but it serves as a benchmark for the performance of the other two models.

3.5 Simulation process

The purpose of each of the three models above is to approximate the geometry of the generating curve of a surface of revolution given a set of marker points, and provide a means by which to compute the force on each marker point. Knowing how to reconstruct the geometry and compute the force allows us to simulate the deformation of the surface over time. Because the force is a nonlinear function of the marker point positions and material data, iterative methods may be used to find the equilibrium state where the force is zero. Our simulation uses the following steps.

1. Generate some initial configuration of marker points and patches. Compute the intrinsic material data for each patch.
2. Simulate the deformation under tension and pressure:
   (a) Run an ODE solver to move the points according to the computed force, until within a certain tolerance.
   (b) Use the output of the ODE solver as the initial guess for a nonlinear solver in order to find the solution.
3. Starting with the final state of the membrane from the previous step, add external force and simulate the movement again using the same procedure.
4. Output images or videos, measure mechanical or geometric data, etc.

3.6 Qualitative remarks

Our software implementation of the simulation is capable of producing videos showing the movement of the surface over time. From these videos, we can make a few qualitative remarks about the models. The linear and parabolic models produce visually similar movements, and the dynamics of strains and tension over time appear similar between the two models.

In both models, strains and tension appear to vary smoothly with respect to both time and position on the generating curve. We also observe that at the tip, the meridional strain equals the circumferential strain, and similarly for the tensions, showing that the tip is isotropic. This evidence all suggests that our models achieve the tip isotropy of the Yanagisawa et al. finite-element model [Yan+15] while avoiding the numerical issues encountered in that paper.

The parabolic arcs model is also more robust to external force. Although both models are capable of handling some external force, the parabolic arcs model can converge to an equilibrium state when a large force is concentrated over a small neighborhood of the tip, while the linear segments model fails. This characteristic alone may make the parabolic arcs model more useful than the linear segments model in cases where large external forces are in play.

4 Force residue analysis on a sphere

4.1 The spherical steady state

In general, it is difficult to find exact solutions to the local force-balance equation (1) from some given initial configuration. However, in the special case where the surface is initially a sphere, such an exact solution can be obtained. Assume that pressure and bulk and shear moduli are all 1, i.e. $P = K_h = \mu_h = 1$. If the initial configuration of the membrane without turgor pressure is a sphere of radius 1, then after turgor pressure is added we expect the membrane to expand uniformly to another sphere of some radius R. Therefore, finding the steady state in this case boils down to finding the right value of R.

In order to make sense of Equation 1 on the deformed sphere, we need to compute σ_s and σ_θ. By a geometric argument, the meridional strain ratio $\lambda_s = ds/ds^0$ is exactly R; the expansion from a sphere of radius 1 to one of radius R increases the arclength everywhere by a factor of R. For the circumferential strain ratio $\lambda_\theta = r/r_0$, note that the point $(\cos\theta, \sin\theta)$ in the initial configuration moves to coordinates $(R\sin\theta, R\cos\theta)$, so $\lambda_\theta = R\cos\theta/\cos\theta = R$. In brief terms, the expansion is isotropic. Recalling that $\mu_h = K_h = 1$, we get

$$\sigma_s = \frac{1}{2}\mu_h\left(\left(\frac{1}{\lambda_\theta}\right)^2 - \left(\frac{1}{\lambda_s}\right)^2\right) + K_h\left(\lambda_s\lambda_\theta - 1\right) = R^2 - 1,$$

$$\sigma_\theta = \frac{1}{2}\mu_h\left(\left(\frac{1}{\lambda_s}\right)^2 - \left(\frac{1}{\lambda_\theta}\right)^2\right) + K_h\left(\lambda_s\lambda_\theta - 1\right) = R^2 - 1.$$

In other words, $\sigma_s = \sigma_\theta = R^2 - 1$ everywhere on the patch. We also need to know the tangent and normal vectors to each point $(R\cos\theta, R\sin\theta)$ on the curve; by simple geometric reasoning these are

$$\hat{t} = \langle \sin\theta, -\cos\theta \rangle,$$

$$\hat{n} = \langle \cos\theta, \sin\theta \rangle.$$

Parametrize the expanded sphere by the angle θ which is formed by the $\hat{z}$-axis and the vector $(R\cos\theta, R\sin\theta)$ corresponding to a point on the sphere. In this setup the arclength element ds transforms as $ds = Rd\theta$. Now, fix $\theta \in [0, \frac{\pi}{2}]$ and let γ be arbitrarily small. We will integrate the left-hand side of Equation 1 over the arc of the circle whose boundaries correspond to angles of $\theta - \gamma$ and $\theta + \gamma$ with the $\hat{z}$-axis. Working

term-by-term,

$$
\begin{aligned}
S_1 &= \int_{\theta=\theta-\gamma}^{\theta=\theta+\gamma} \frac{d(\sigma_s \hat{t})}{ds}\, ds && (18)\\
&= (\sigma_s \langle \sin\theta, -\cos\theta \rangle)|_{\theta-\gamma}^{\theta+\gamma} \\
&= (R^2-1)\langle \sin(\theta-\gamma) - \sin(\theta+\gamma), \cos(\theta-\gamma) + \cos(\theta+\gamma)\rangle, \\
S_2 &= \int_{\theta=\theta-\gamma}^{\theta=\theta+\gamma} \frac{(\sigma_s - \sigma_\theta)\hat{r}}{r(s)}\, ds && (19)\\
&= \int_{\theta=\theta-\gamma}^{\theta=\theta+\gamma} 0\hat{r}\, ds \\
&= \langle 0, 0\rangle, \\
S_3 &= \int_{\theta=\theta-\gamma}^{\theta=\theta+\gamma} \frac{-\sigma_s \sin\alpha}{r(s)}\, ds \quad (\alpha \text{ is the angle from } \hat{r} \text{ to } \hat{t}) && (20)\\
&= \int_{\theta-\gamma}^{\theta+\gamma} \frac{-\sigma_s \sin\theta}{R\sin\theta} \langle \cos\theta, \sin\theta\rangle R\, d\theta \\
&= (R^2-1)\langle \sin(\theta-\gamma) - \sin(\theta+\gamma), \cos(\theta-\gamma) + \cos(\theta+\gamma)\rangle, \\
S_4 &= \int_{\theta=\theta-\gamma}^{\theta=\theta+\gamma} P\hat{n}(s)\, ds && (21)\\
&= \int_{\theta-\gamma}^{\theta+\gamma} \langle \cos\theta, \sin\theta\rangle R\, d\theta \\
&= -R\langle \sin(\theta-\gamma) - \sin(\theta+\gamma), \cos(\theta-\gamma) + \cos(\theta+\gamma)\rangle
\end{aligned}
$$

So overall, integrating the force balance equation over the small arc from $\theta-\gamma$ to $\theta+\gamma$ yields

$$S_1 + S_2 + S_3 + S_4 = (2(R^2-1) - R)\langle \sin(\theta-\gamma) - \sin(\theta+\gamma), \cos(\theta-\gamma) + \cos(\theta+\gamma)\rangle = \langle 0, 0\rangle. \quad (22)$$

This means that the steady-state radius R must satisfy $2R^2 - R - 2 = 0$. This equation has only one positive solution, $R = \frac{1}{4}(1+\sqrt{17}) \approx 1.2808$. In other words, we have found that when turgor pressure is added to to the sphere of radius 1, the membrane expands to a sphere of radius $\frac{1}{4}(1+\sqrt{17})$.

4.2 Steady state force residue under each model

Here we present the computed force in the exact steady state under each of the three models. If the models were perfect, the computed force would be zero; this is not the case, however, and the norm of the computed force at each marker point measures the model's error at that location. For the purposes of this analysis, we use a system with $N = 16$ patches bordered by 17 marker points, distributed evenly on a quarter-circle of radius $R = \frac{1}{4}(1+\sqrt{17})$. We expect to see evidence supporting the following hypotheses:

- The parabolic arcs model should have the smallest error, followed by the linear segments model, and the degenerate parabolic arcs model should have the largest error.
- The computed forces under each method should be sensitive to K_h but not μ_h.

Figures 3b, 3a, and 3c show the force residue under each model with material parameters $K_h = 1$ and $\mu_h = 1$. Note that the color scale is *not* consistent among each figure.

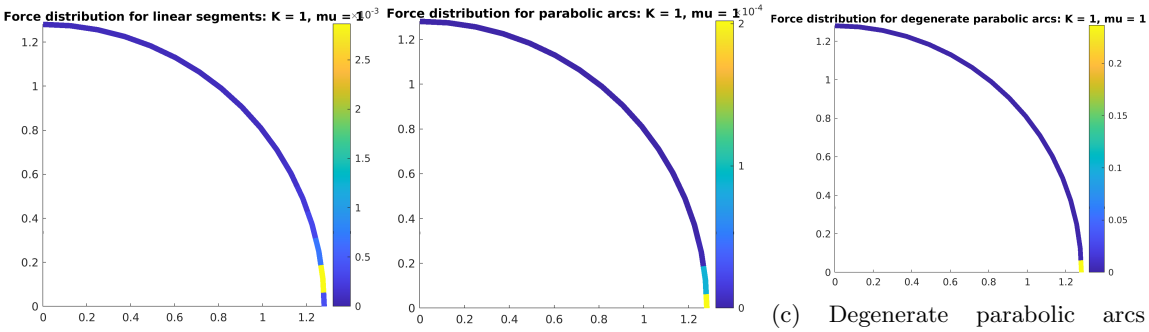

(a) Linear segments model (b) Parabolic arcs model (c) Degenerate parabolic arcs model

Figure 3: Force residue on the steady sphere with $K_h = 1$, $\mu_h = 1$.

Here we see that the relationships of the errors under the three force computation methods do indeed fit our expectations: the parabolic arcs model slightly beats the linear one, while the model based on degenerate parabolic arcs has error on the order of 1000 times the other methods at its worst point.

By comparing Figures 3b, 3a, and 3c with Figures 4b, 4a, and 4c, we observe that the computed forces on the sphere are not sensitive to μ_h.

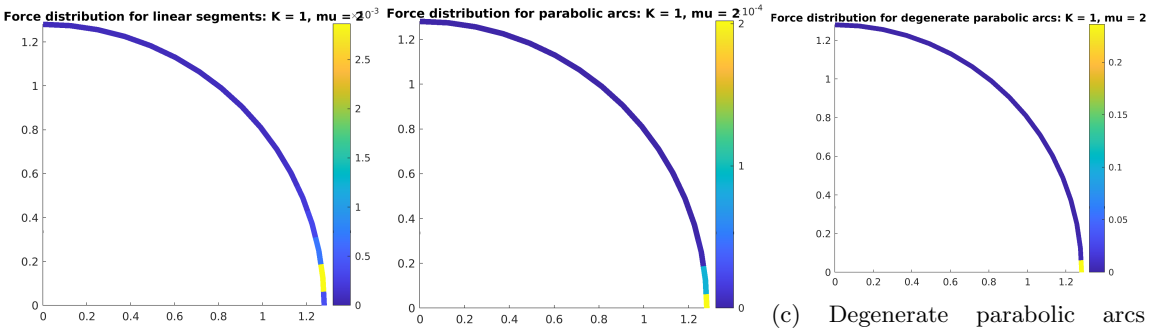

(a) Linear segments model (b) Parabolic arcs model (c) Degenerate parabolic arcs model

Figure 4: Force residue on the steady sphere with $K_h = 1$, $\mu_h = 2$.

However, comparing Figures 3b, 3a, and 3c with Figures 5b, 5a, and 5c suggests that the computed forces are sensitive to K_h.

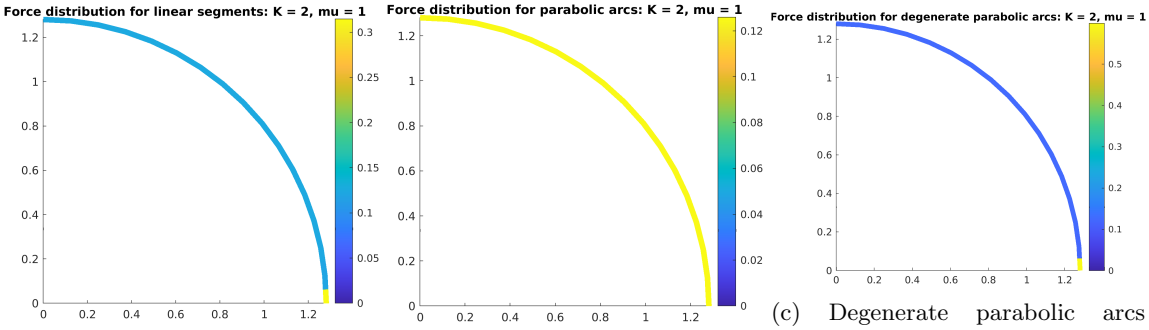

(a) Linear segments model (b) Parabolic arcs model (c) Degenerate parabolic arcs model

Figure 5: Force residue on the steady sphere with $K_h = 2$, $\mu_h = 1$.

Even with increased K_h, the parabolic model still appears to slightly outperform the linear model in some respects, and the degenerate parabolic arcs model still has worse error than the other two. Overall, we find that the force computations provide evidence for our hypotheses and strongly suggest that the simulation based on parabolic arcs will be more accurate than that based on linear segments.

4.3 Orders of accuracy for force residue in the steady state

By increasing the number of patches in the simulation, we can analyze how the error in the computed force responds to finer discretization. To generate the following plots we set $K_h = 1$ and $\mu_h = 1$, and compute the force residue in the exact steady state for 16, 32, 64, and 128 patches. For the order of accuracy of the overall force, we construct the overall force vector by assembling the two force components on each of the $N + 1$ points into a vector (where N is the number of patches), and discard the $\hat{z}$-component at the rear point and the $\hat{r}$-component at the tip point. This produces a $2N$-component vector, and we quantify the overall error in the computed force by the 2-norm or ∞-norm of this vector.

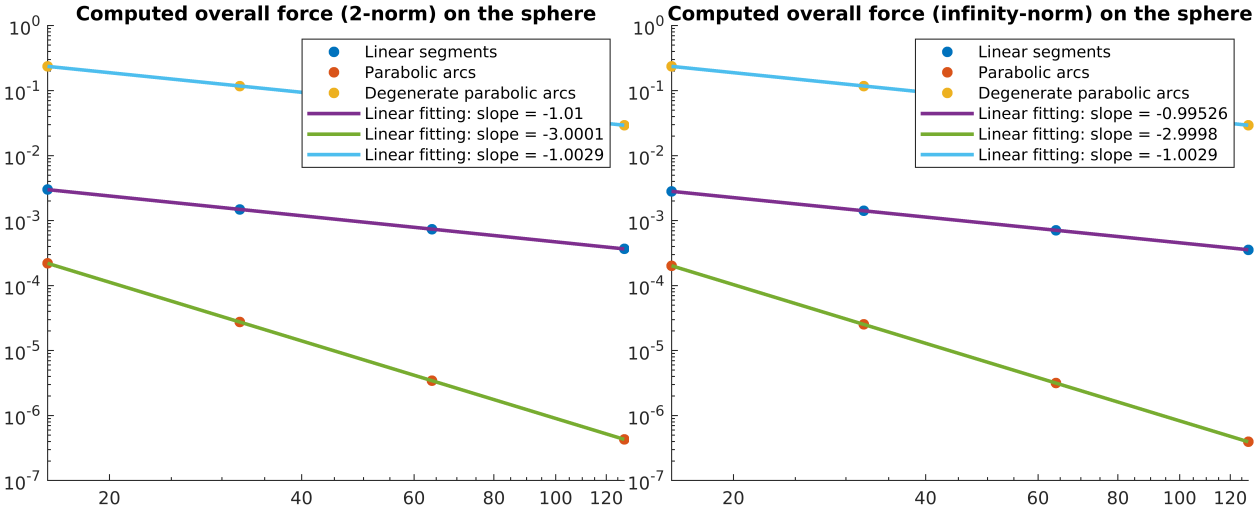

(a) 2-norm (b) ∞-norm

Figure 6: Plot of the error in the overall force computation for the three models under 2-norm and ∞-norm. The x-axis is the number of patches (log scale) and the y-axis is the norm of the overall force vector.

Figures 6a and 6b show that for the overall force on all marker points, the order of accuracy of the parabolic arcs model is roughly 3. This is an improvement compared to the linear segments model, which has order of accuracy about 1.

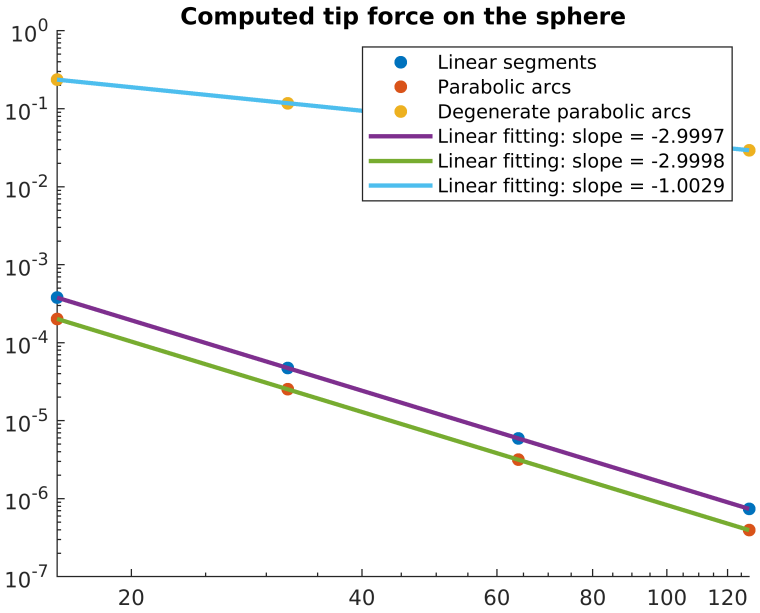

Figure 7: Plot of the error in the tip force computation for the three methods. The x-axis is the number of patches (log scale) and the y-axis is the norm of the force at the tip.

Figure 7 shows the force at the tip for each of the the methods. The norm is not specified because the force at the tip has only one nonzero component. The figure shows that tip force in the parabolic arcs model and linear segments model are both about 3rd-order accurate.

In Figures 6 and 7 we also observe that the degenerate parabolic arcs model shows order of accuracy approximately 1 for both tip force residue and overall force residue. This indicates that this model should perform worse overall than the other two models, and this claim is supported by evidence from the simulations. We will refrain from discussing the the degenerate parabolic arcs model until Section 6, where the degenerate parabolic model will serve as a useful comparison for the other models.

4.3.1 Explanation for similar tip behavior in the linear and parabolic models

The similar order of accuracy for tip force in the linear and parabolic models is somewhat surprising because the geometry around the tip is assumed to be different. For the model based on linear segments the tip is assumed conical, while in the parabolic arcs model the tip is assumed to be a paraboloid. However, we will show that (up to a couple of reasonable approximations) the tip force relations are essentially the same for both models.

Assume that $\sigma_s = \sigma_\theta$ are constant in a neighborhood of the tip. Firstly, in the linear segments case, we specify the force at the tip as follows using the tip boundary condition (Equation 6):

$$\begin{cases} F_z = -\sigma_s \sin(\gamma^{N+1/2}) + Pr(s^{N+1/2})/2, \\ F_r = 0, \end{cases} \tag{23}$$

where $\gamma^{N+1/2}$ is the angle formed by the $\hat{r}$ basis vector and the tangent vector of the linear segment which precedes the tip point. (In other contexts this is called α; we diverge from the convention here to avoid confusion with what follows.)

Now consider the parabolic model. Let $s^{N+1/2}$, $t^{N+1/2}$ ($s^{N+3/2}$, $t^{N+3/2}$) be the arclength and time corresponding to the midpoint by arclength of the patch immediately preceding (following) the tip point.

Importantly, we note that $t^{N+1/2} < 0 < t^{N+3/2}$. We will integrate the local force

$$\underbrace{\frac{d(\sigma_s \hat{t})}{ds}}_{(1)} + \underbrace{\frac{\sigma_s - \sigma_\theta}{r}\hat{r}}_{(2)} - \underbrace{\frac{\sigma_s \sin\alpha(s)}{r}\hat{n}}_{(3)} + \underbrace{P\hat{n}}_{(4)}$$

from $s^{N+1/2}$ to $s^{N+3/2}$, taking advantage of the symmetry of the patches preceding and following the tip point, and also keeping in mind the construction of these patches from a parabola opening along the $\hat{z}$-axis (see Section 3.3.4). We note that

$$\cos(\alpha(t)) = \frac{\cos(\alpha^{N+1/2}) + 2t\sin(\alpha^{N+1/2})/\mathrm{sgn}(\lambda)\lambda^2}{\sqrt{1+\frac{4t^2}{\lambda^4}}}.$$

Since $\alpha^{N+1/2} = \pi$ by construction, this simplifies to

$$\cos(\alpha(t)) = \frac{-1}{\sqrt{1+\frac{4t^2}{\lambda^4}}}.$$

By a similar computation,

$$\sin(\alpha(t)) = \frac{-2t/\mathrm{sgn}(\lambda)\lambda^2}{\sqrt{1+\frac{4t^2}{\lambda^4}}}.$$

We will integrate each term of the local force separately, assuming for convenience that the parabolic stretch factor λ for the tip patch is positive.

$$S_1 = \int_{s^{N+1/2}}^{s^{N+3/2}} \frac{d(\sigma_s \hat{t})}{ds}\, ds = \sigma_s(\hat{t}(s^{N+3/2}) - \hat{t}(s^{N+1/2})) \tag{24}$$
$$= \left\langle 2\sigma_s \sin(\alpha(s^{N+1/2})), 0 \right\rangle = \left\langle 2\sigma_s \frac{t^{N+1/2}}{\sqrt{\frac{\lambda^4}{4} + (t^{N+1/2})^2}}, 0 \right\rangle,$$

$$S_2 = \int_{s^{N+1/2}}^{s^{N+3/2}} \frac{\sigma_s - \sigma_\theta}{r(s)}\hat{r}\, ds = \langle 0, 0\rangle \quad \text{(by symmetry)}, \tag{25}$$

$$S_3 = \int_{s^{N+1/2}}^{s^{N+3/2}} \frac{-\sigma_s \sin\alpha(s)}{r(s)}\hat{n(s)}\, ds = \int_{t^{N+1/2}}^{t^{N+3/2}} \frac{-\sigma_s \cdot -2t/\lambda^2}{-t} \langle -\cos(\alpha(t)), \sin(\alpha(t))\rangle\, dt \tag{26}$$
$$= \left\langle \frac{-4\sigma_s}{\lambda^2} \int_{t^{N+1/2}}^{t_{N+1}} \left(1 + \frac{4t^2}{\lambda^4}\right)^{-1/2} dt, 0 \right\rangle = \left\langle -2\sigma_s \int_{t^{N+1/2}}^{0} \left(\frac{\lambda^4}{4} + t^2\right)^{-1/2} dt, 0 \right\rangle$$
$$= \left\langle 2\sigma_s \mathrm{arctanh}\left(\frac{t^{N+1/2}}{\sqrt{\frac{\lambda^4}{4} + (t^{N+1/2})^2}}\right), 0 \right\rangle,$$

$$S_4 = \int_{s^{N+1/2}}^{s^{N+3/2}} P\hat{n}\, ds = P\int_{t^{N+1/2}}^{t^{N+3/2}} \hat{n}(t)\sqrt{1 + \frac{4t^2}{(\lambda^{i-1/2})^4}}\, dt \tag{27}$$
$$= P\int_{t^{N+1/2}}^{t^{N+3/2}} \sqrt{1 + \frac{4t^2}{(\lambda^{i-1/2})^4}}\, \langle -\cos(\alpha(t)), \sin(\alpha(t))\rangle\, dt$$
$$= \left\langle 2P\int_{t^{N+1/2}}^{t_{N+1}} -\cos(\alpha(t))\sqrt{\frac{4t^2}{(\lambda^{i-1/2})^4}}\, dt, 0 \right\rangle = \left\langle 2P\int_{t^{N+1/2}}^{0} 1\, dt, 0 \right\rangle = \left\langle 2P|t^{N+1/2}|, 0 \right\rangle.$$

Therefore, the total force at the tip is

$$F = \left\langle 2\sigma_s \left(\frac{t^{N+1/2}}{\sqrt{\frac{\lambda^4}{4} + (t^{N+1/2})^2}} + \operatorname{arctanh}\left(\frac{t^{N+1/2}}{\sqrt{\frac{\lambda^4}{4} + (t^{N+1/2})^2}} \right) \right) + 2P|t^{N+1/2}|, 0 \right\rangle.$$

Here we make our first approximation. For a fine enough discretization, $\frac{t^{N+1/2}}{\sqrt{\frac{\lambda^4}{4}+(t^{N+1/2})^2}}$ will be small, so

$$\operatorname{arctanh}\left(\frac{t^{N+1/2}}{\sqrt{\frac{\lambda^4}{4} + (t^{N+1/2})^2}} \right) \approx \frac{t^{N+1/2}}{\sqrt{\frac{\lambda^4}{4} + (t^{N+1/2})^2}}.$$

Therefore

$$F \approx \left\langle 4\sigma_s \frac{t^{N+1/2}}{\sqrt{\frac{\lambda^4}{4} + (t^{N+1/2})^2}} + 2P|t^{N+1/2}|, 0 \right\rangle.$$

To further handle this quantity, we need to make sense of λ. On the tip patch, if p denotes the tip point and q the preceding marker point, we defined

$$\lambda = \frac{q_r}{\sqrt{p_z - q_z}}.$$

If we denote by $(\Delta z, \Delta r)$ the vector which forms the linear segment preceding the tip point, then

$$\lambda = \frac{\Delta r}{\sqrt{\Delta z}}.$$

For a fine enough discretization, we will have $\Delta r \approx 2|t^{N+1/2}|$, because $|t^{N+1/2}|$ corresponds to the midpoint of the parabolic arc by its arclength. Therefore,

$$\frac{\lambda^4}{4(t^{N+1/2})^2} = \frac{\Delta r^4}{\Delta z^2 \cdot 4(t^{N+1/2})^2} \approx \frac{\Delta r^4}{\Delta z^2 \Delta r^2} = \frac{\Delta r^2}{\Delta z^2} = \frac{\cos^2(\gamma)}{\sin^2(\gamma)}.$$

Recalling that $t^{N+1/2} < 0$, this gives

$$\frac{t^{N+1/2}}{\sqrt{\frac{\lambda^4}{4} + (t^{N+1/2})^2}} = \frac{-1}{\sqrt{\frac{\lambda^4}{4(t^{N+1/2})^2} + 1}} \approx \frac{-1}{\sqrt{\frac{\cos^2(\gamma^{N+1/2})}{\sin^2(\gamma^{N+1/2})} + 1}} = -\sin(\gamma^{N+1/2}),$$

and thus we obtain

$$F \approx \left\langle -4\sigma_s \sin(\gamma^{N+1/2}) + 2P|t^{N+1/2}|, 0 \right\rangle = \left\langle -4\sigma_s \sin(\gamma^{N+1/2}) + 2Pr(s^{N+1/2}), 0 \right\rangle. \tag{28}$$

The right-hand side is equal to 0 exactly when $F = 0$ in the linear case. This explains the similar orders of accuracy at the tip for the linear and parabolic models.

5 Convergence analyses

In this section we demonstrate the convergence of the linear segments model and the parabolic arcs model and we show the order of accuracy for each. Throughout this section, we set the physical parameters $P = K_h = \mu_h = 1$.

5.1 Convergence analysis for spheres

For an initial spherical configuration, the exact steady state is known (see Section 4.1). Therefore, we can compute the error in the simulated steady state by comparing with the marker point positions and the tensions in the exact steady state discretized in the corresponding manner. For a system with N patches, we take the positional error to be the norm of the difference in marker points position vectors (a $2N$-vector, disregarding the rear $\hat{z}$-component and the tip $\hat{r}$-component), and the meridional (circumferential) tension error to be the norm of the difference in meridional (circumferential) tension vectors (an N-vector).

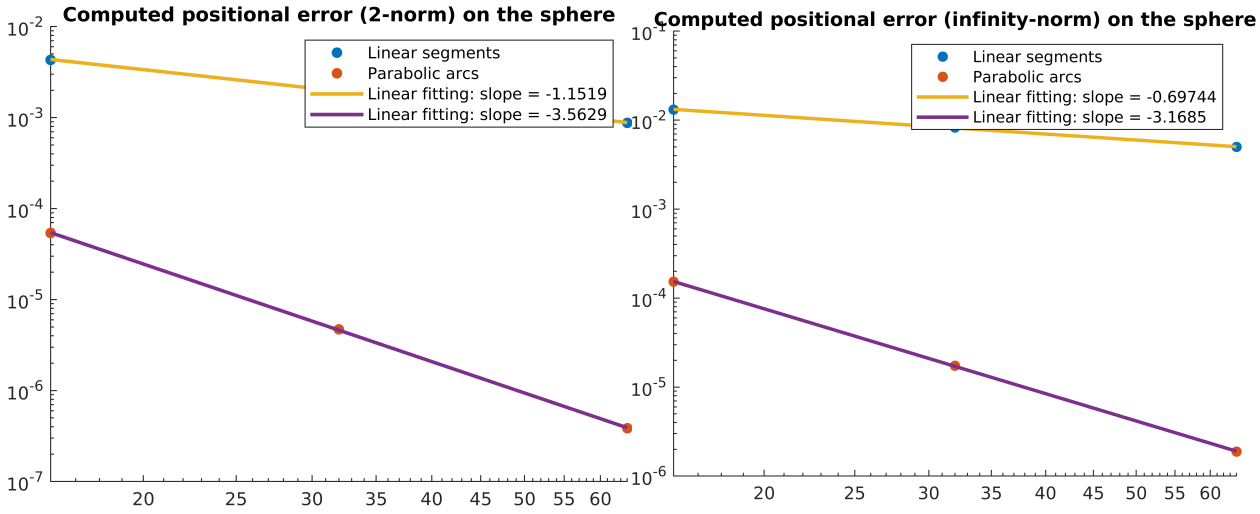

(a) 2-norm

(b) ∞-norm

Figure 8: Plot of the error in the positions of marker points for the two methods under 2-norm and ∞-norm. The x-axis is the number of patches (log scale) and the y-axis is the norm of the overall positional error vector.

Figure 8 shows that the order of accuracy for marker points in the linear model is roughly $0.7 - 1.2$, while under the parabolic model the order of accuracy is roughly $3.2 - 3.6$, depending on the norm used. Hence the parabolic model shows significantly better convergence.

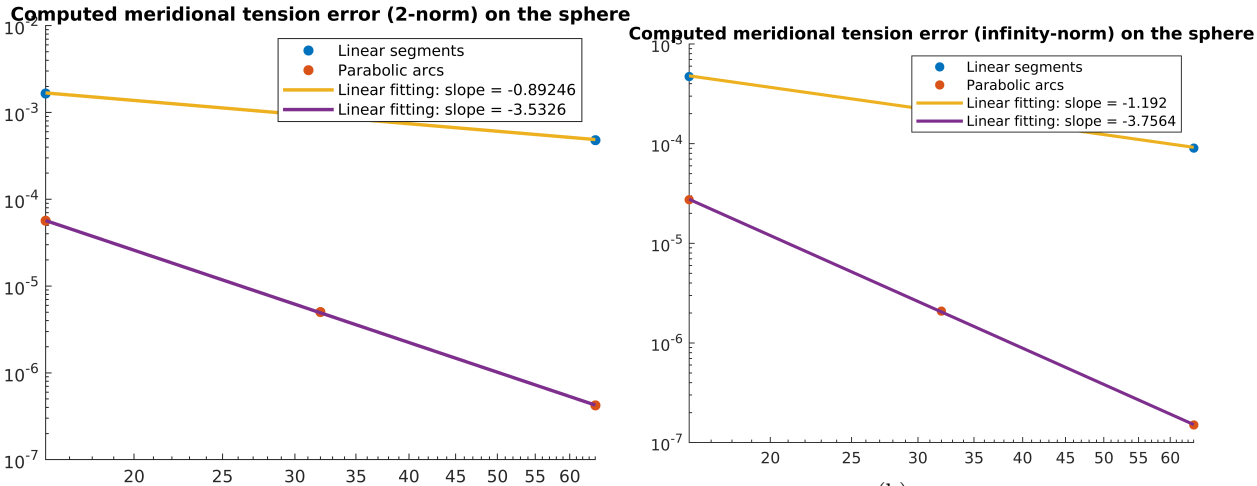

(a) 2-norm

(b) ∞-norm

Figure 9: Plot of the error in the meridional tension for the two methods under 2-norm and ∞-norm. The x-axis is the number of patches (log scale) and the y-axis is the norm of the overall meridional tension error vector.

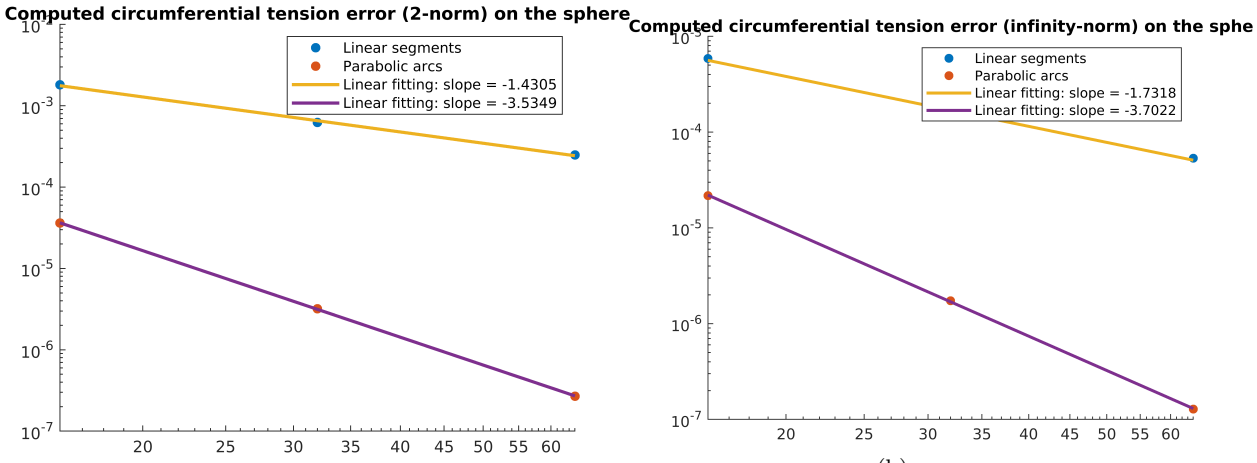

(a) 2-norm

(b) ∞-norm

Figure 10: Plot of the error in the circumferential tension for the two methods under 2-norm and ∞-norm. The x-axis is the number of patches (log scale) and the y-axis is the norm of the overall circumferential tension error vector.

Figure 9 shows that the order of accuracy for meridional tension in the linear segments model is roughly $0.9 - 1.2$, while in the parabolic arcs model the order of accuracy is roughly $3.5 - 3.8$. Similarly, for circumferential tension, we see in Figure 10 that the linear model has order of accuracy roughly $1.4 - 1.7$, while the parabolic model has order of accuracy roughly $3.5 - 3.7$. So again the parabolic arcs model has better convergence than the linear model for spherical initial configuration.

5.2 Convergence analysis for ellipses

In this section, we discuss the convergence properties of the linear and parabolic models when the initial configuration is an ellipse. Suppose that the ellipse's half-width in the $\hat{z}$-direction is a and its half-width in the $\hat{r}$-direction is b. In contrast with the spherical case, the exact steady state in this case is not known. We will perform the same analysis as in the spherical case, but to measure the error we compute the numerical solutions for 2^n, 2^{n+1}, ..., 2^{n+k} patches (we require $k \geq 2$). Then we measure error as the norm of the computed solution for 2^{n+i} patches minus the computed configuration for 2^{n+k} patches, that is, we take the highest-resolution simulation as the true steady state. This will introduce a bias toward convergence for each model, but we can still use these figures to compare the performance of the models against each other

To deal with the fact that the highest-resolution solution has more points and patches than the other computed solutions, we trim the set of marker points coming from the highest-resolution solution in the following way. Suppose we want to compute the error for a simulation on 2^{n+i} patches. Recalling that the high-resolution solution involved 2^{n+k} marker points, we select its first element and every 2^{k-i}-th element thereafter. For example, if $i = 1$, the list of points

$$(1,1),(2,2),(3,3),(4,4),(5,5),(6,6),(7,7),(8,8),(9,9)$$

corresponding to $k = 3$ is trimmed to

$$(1,1),(5,5),(9,9).$$

For tensions, we employ an averaging method. In this case, we take the list of 2^{n+k} tensions (one for each patch) and to produce the averaged tension list of length 2^{n+i}, we average groups of 2^{k-i} consecutive values. So, again taking $i = 1$ as the example, the tension list

$$1,2,3,4,5,6,7,8$$

corresponding to $k = 3$ is averaged to

$$2.5, 6.5.$$

Note that our tension averaging scheme doesn't take into account the size of the patches. From a physical point of view, it may make sense to average the tensions using a weighting scheme which gives higher weight to the larger patches; we disregard this consideration in our analysis.

Figures 11 and 12 show the estimated order of accuracy for marker point positions on some ellipses in the linear and parabolic schemes. These figures show higher order of accuracy for the linear segments model than in the spherical case; this is because the selection of a computed high-resolution steady state as the true steady state might induce a bias toward apparent convergence. In the case where the ellipse is a circle, we recover the high order of accuracy as before. However, when the ellipse has nonzero eccentricity, the orders of accuracy for both methods deteriorate sharply. The parabolic arcs model still seems to outperform the linear segments model by an appreciable margin when the initial ellipse is very wide in the $\hat{r}$-direction compared to the $\hat{z}$-direction. However, in the opposite scenario, i.e. when the initial ellipse is wide in the $\hat{z}$-direction, the improvement of the parabolic arcs model is very minor.

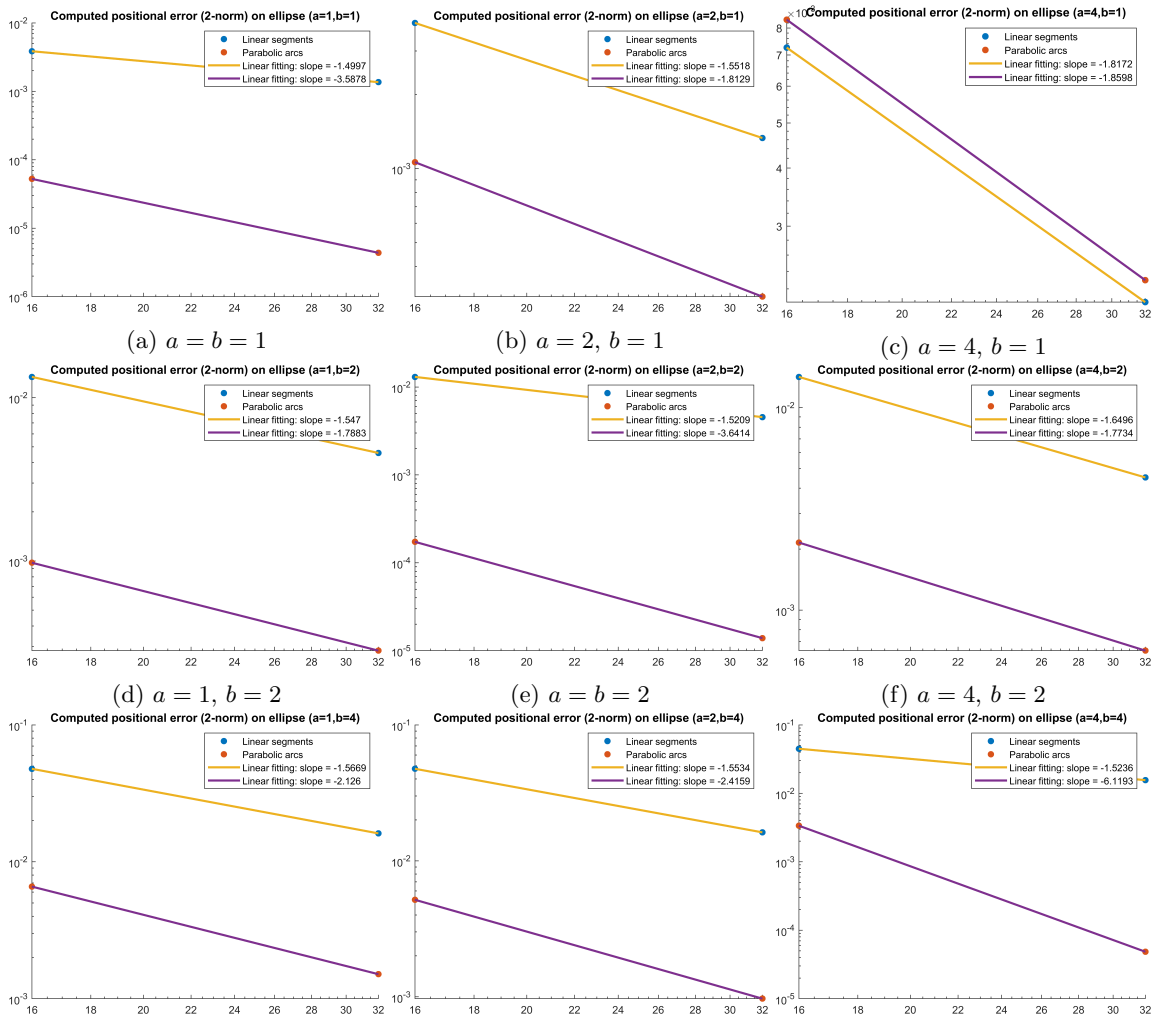

(a) $a = b = 1$ (b) $a = 2,\ b = 1$ (c) $a = 4,\ b = 1$

(d) $a = 1,\ b = 2$ (e) $a = b = 2$ (f) $a = 4,\ b = 2$

(g) $a = 1,\ b = 4$ (h) $a = b = 4$ (i) $a = 4,\ b = 4$

Figure 11: Order of accuracy for marker points on ellipses under 2-norm. Note that the cases $a = b = 1$, $a = b = 2$, and $a = b = 4$ correspond to spheres.

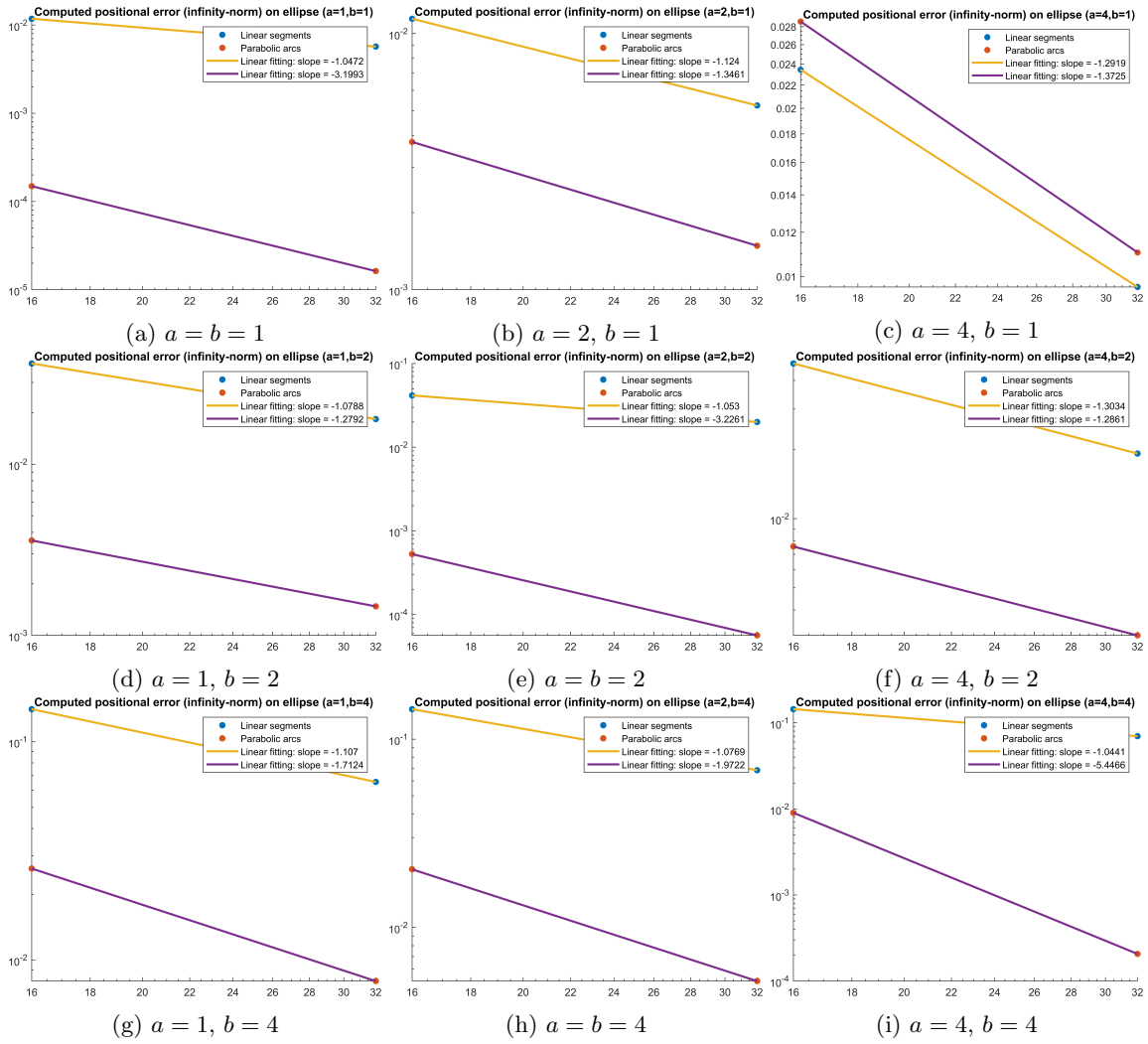

(a) $a = b = 1$ (b) $a = 2,\ b = 1$ (c) $a = 4,\ b = 1$

(d) $a = 1,\ b = 2$ (e) $a = b = 2$ (f) $a = 4,\ b = 2$

(g) $a = 1,\ b = 4$ (h) $a = b = 4$ (i) $a = 4,\ b = 4$

Figure 12: Order of accuracy for marker points on ellipses under ∞-norm. Note that the cases $a = b = 1$, $a = b = 2$, and $a = b = 4$ correspond to spheres.

Figures 13, 14, 15, and 16 show the estimated orders of accuracy for meridional and circumferential tensions on some ellipses in the linear and parabolic schemes. Here we again see that in the case where $a = b$, the high order of accuracy we have already observed for tensions on spheres is recovered. However, when the ellipse is non-circular, the convergence in the parabolic model again deteriorates and is not much better (sometimes even slightly worse) than the linear scheme.

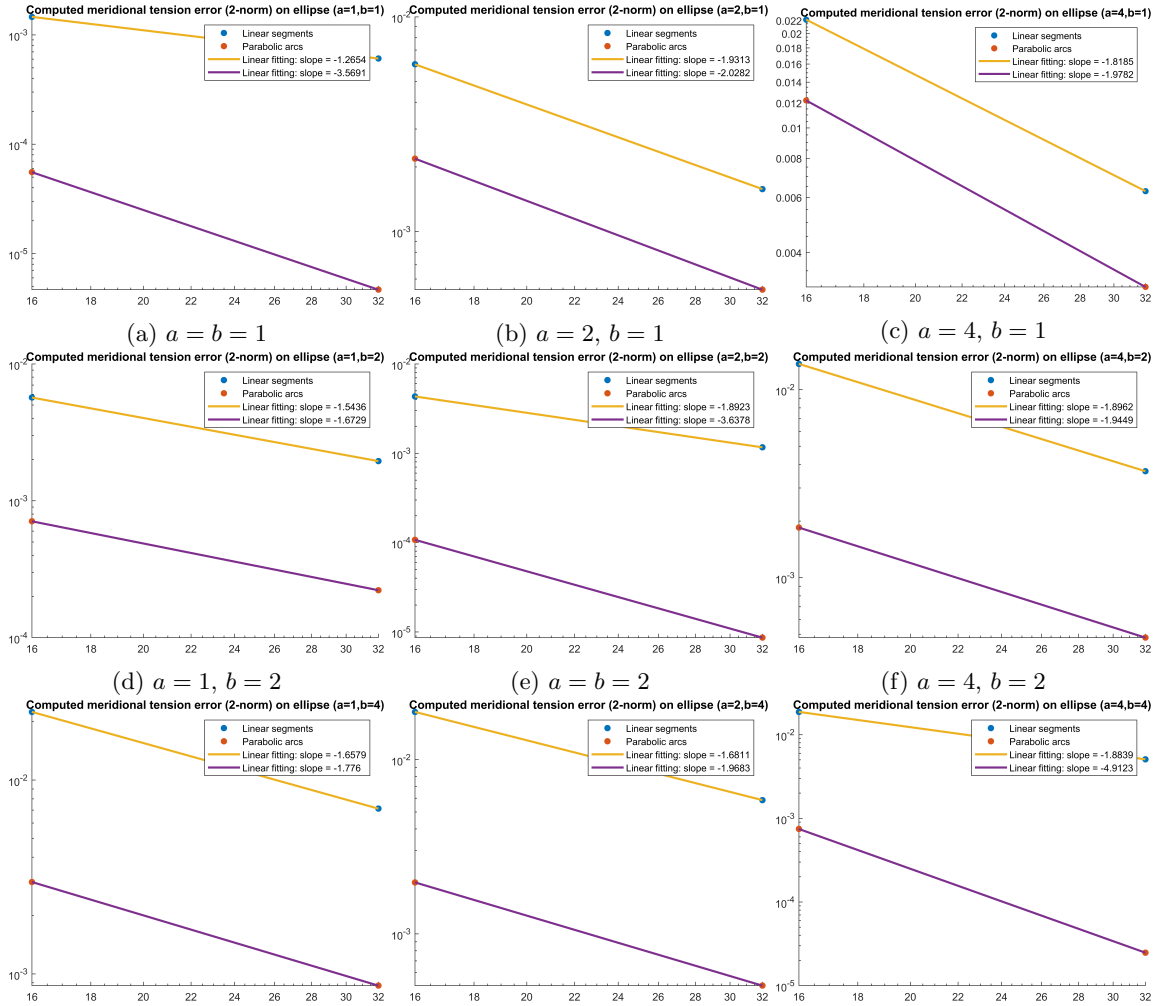

(a) $a = b = 1$ (b) $a = 2,\ b = 1$ (c) $a = 4,\ b = 1$

(d) $a = 1,\ b = 2$ (e) $a = b = 2$ (f) $a = 4,\ b = 2$

(g) $a = 1,\ b = 4$ (h) $a = 2,\ b = 4$ (i) $a = b = 4$

Figure 13: Order of accuracy for meridional tension σ_s on ellipses under 2-norm. Note that the cases $a = b = 1$, $a = b = 2$, and $a = b = 4$ correspond to spheres.

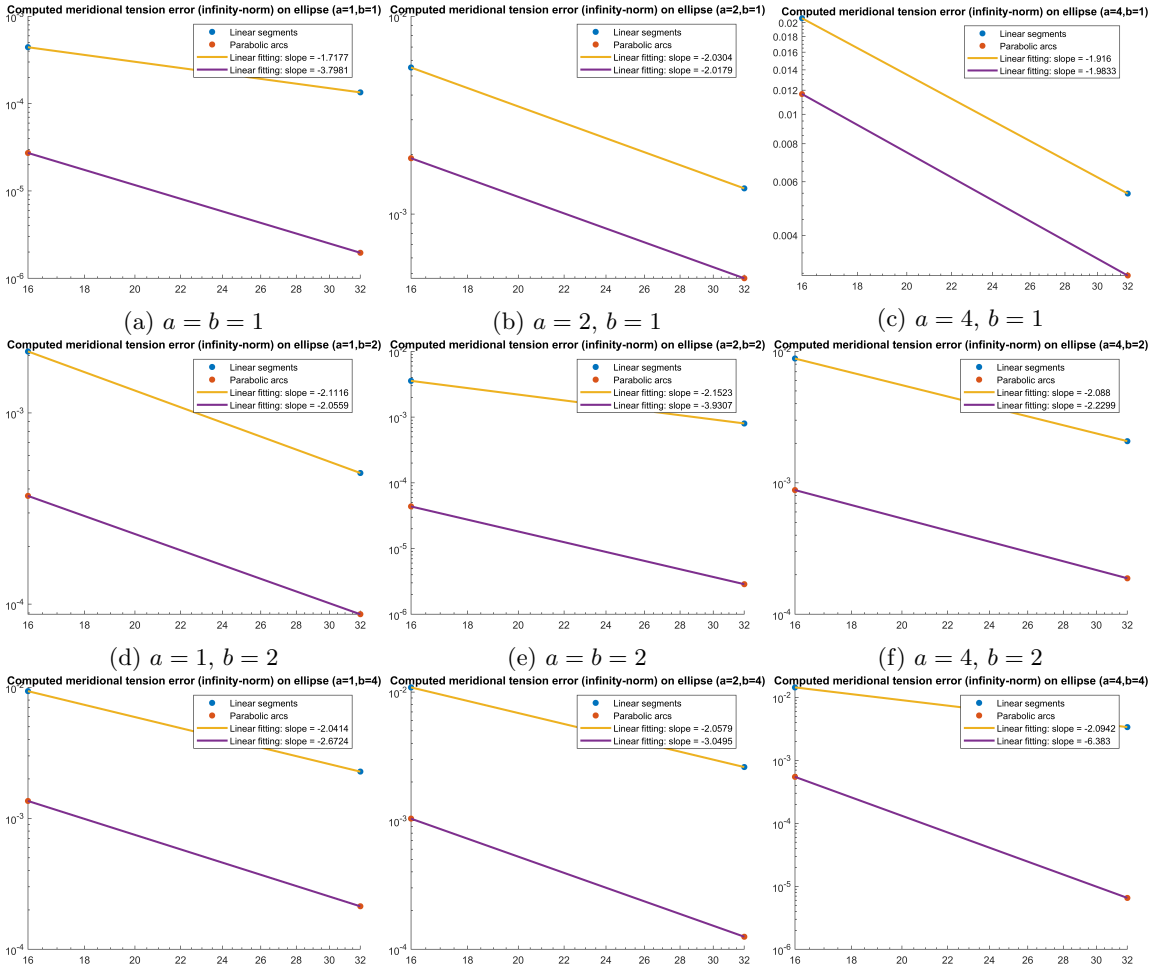

(a) $a = b = 1$ (b) $a = 2,\ b = 1$ (c) $a = 4,\ b = 1$

(d) $a = 1,\ b = 2$ (e) $a = b = 2$ (f) $a = 4,\ b = 2$

(g) $a = 1,\ b = 4$ (h) $a = 2,\ b = 4$ (i) $a = b = 4$

Figure 14: Order of accuracy for meridional tension σ_s on ellipses under ∞-norm. Note that the cases $a = b = 1$, $a = b = 2$, and $a = b = 4$ correspond to spheres.

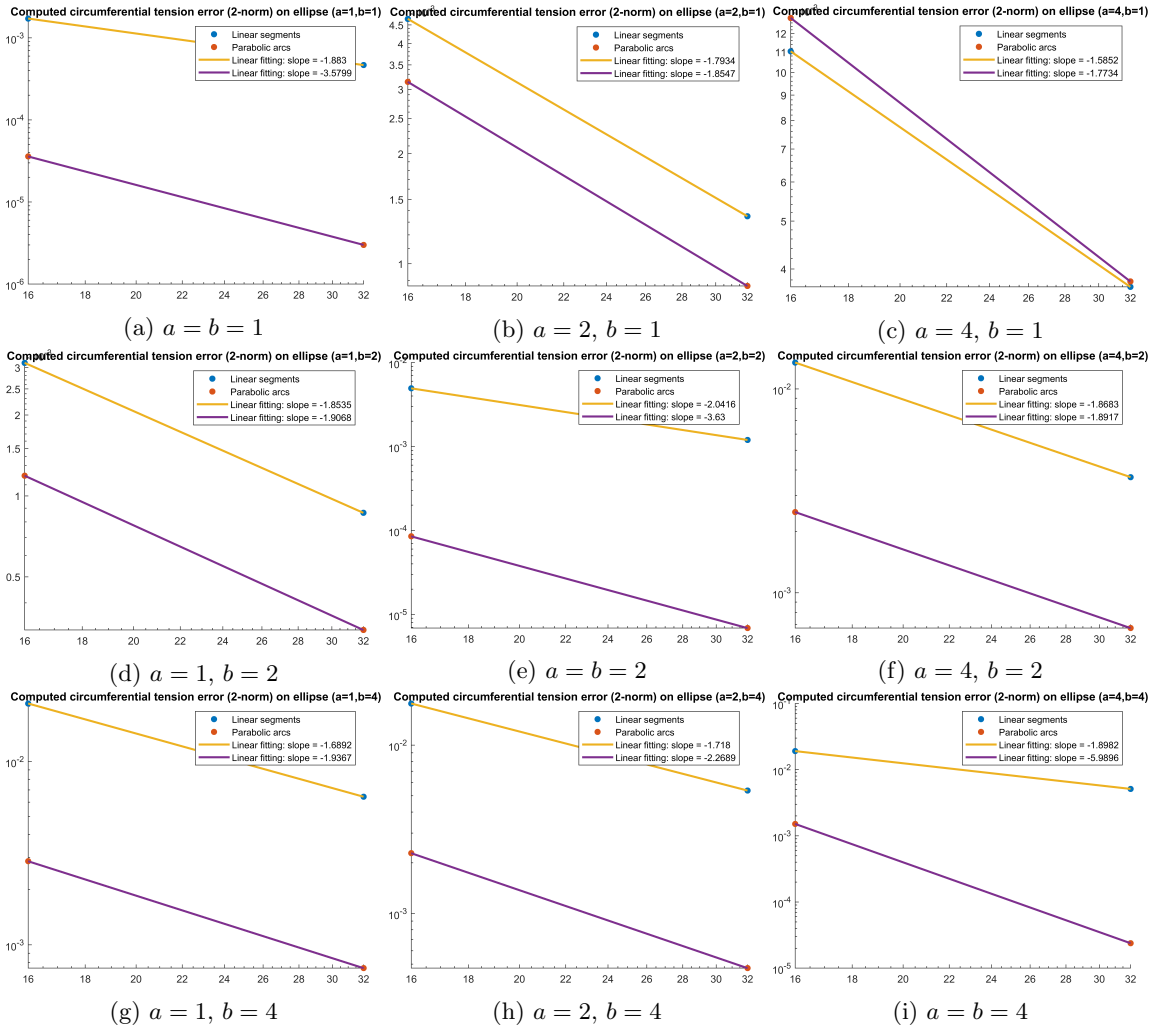

(a) $a = b = 1$ (b) $a = 2,\ b = 1$ (c) $a = 4,\ b = 1$

(d) $a = 1,\ b = 2$ (e) $a = b = 2$ (f) $a = 4,\ b = 2$

(g) $a = 1,\ b = 4$ (h) $a = 2,\ b = 4$ (i) $a = b = 4$

Figure 15: Order of accuracy for circumferential tension σ_θ on ellipses under 2-norm. Note that the cases $a = b = 1$, $a = b = 2$ and $a = b = 4$ correspond to spheres.

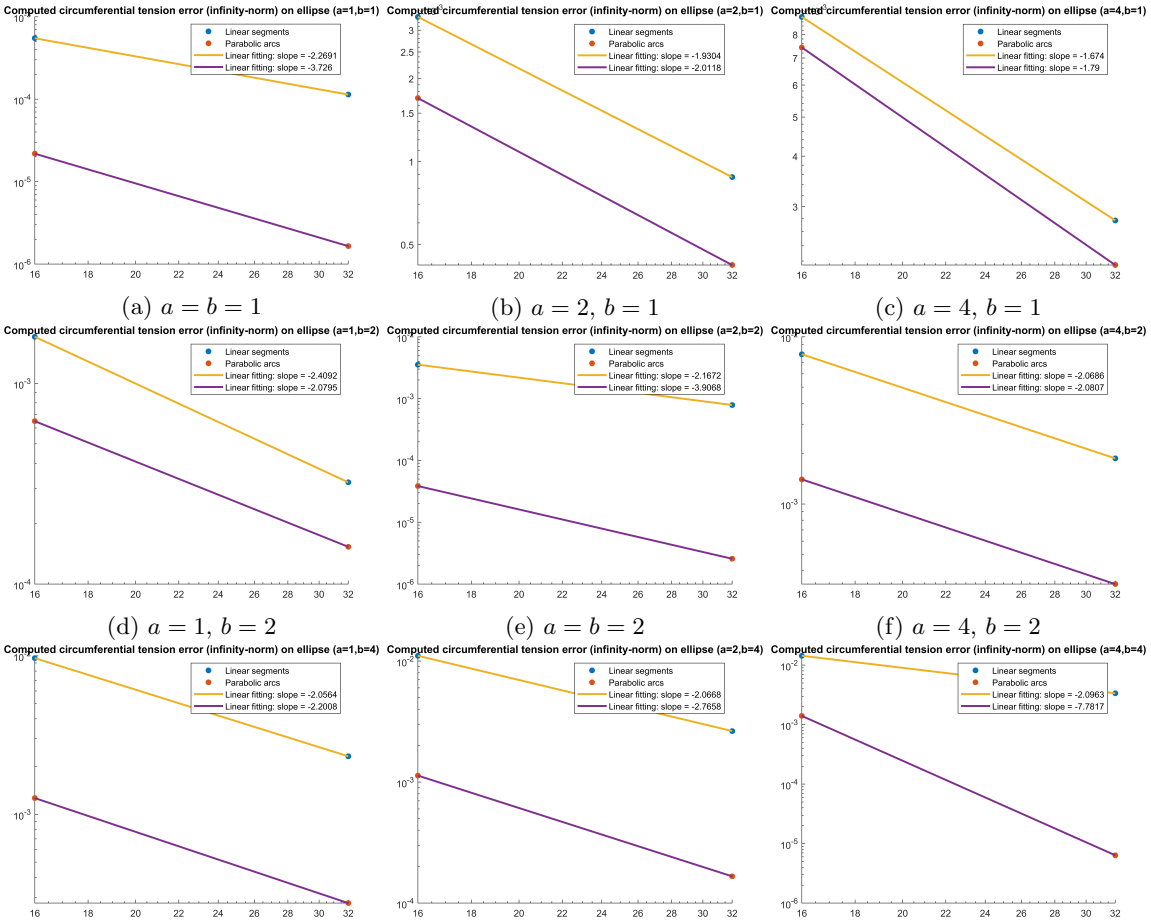

(a) $a = b = 1$ (b) $a = 2,\ b = 1$ (c) $a = 4,\ b = 1$

(d) $a = 1,\ b = 2$ (e) $a = b = 2$ (f) $a = 4,\ b = 2$

(g) $a = 1,\ b = 4$ (h) $a = 2,\ b = 4$ (i) $a = b = 4$

Figure 16: Order of accuracy for circumferential tension σ_θ on ellipses under ∞-norm. Note that the cases $a = b = 1$, $a = b = 2$ and $a = b = 4$ correspond to spheres.

5.3 Remarks on displacement under the parabolic arcs model

Let us return to the example of the initial spherical configuration. Because the points in the initial configuration are evenly distributed with respect to arclength, and the steady solution is a uniformly expanded sphere, we expect the displacement vectors from marker points in the known steady state to marker points in the computed solution to be approximately radial. However, this is not the case; in Figure 17 we show the displacement from the known steady state to the computed solution for each marker point in a system of $N = 8$ patches under the parabolic arcs model. Note that the scale is not uniform among all of the subfigures.

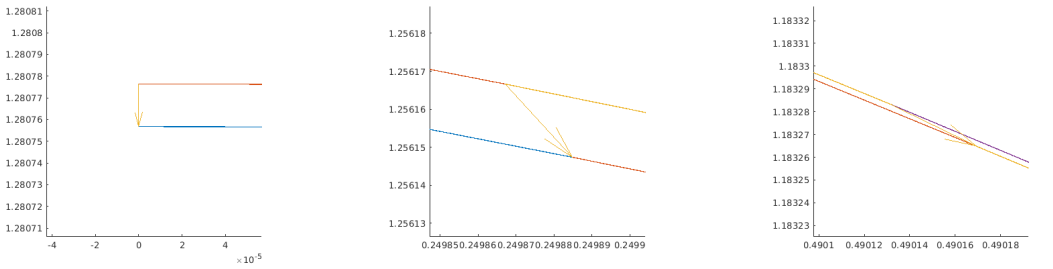

(a) 1st (rear) marker point (b) 2nd marker point (c) 3rd marker point

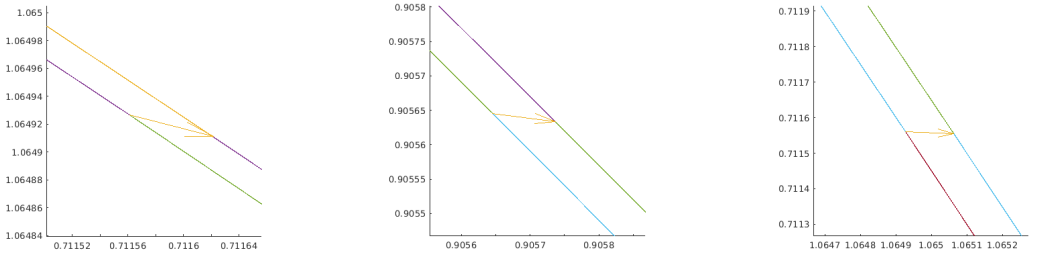

(d) 4th marker point (e) 5th marker point (f) 6th marker point

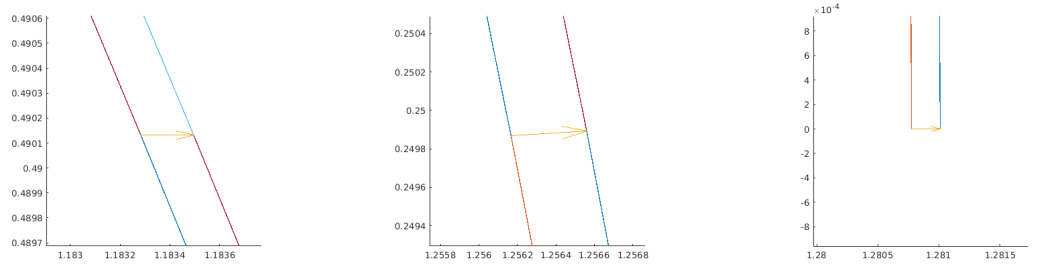

(g) 7th marker point (h) 8th marker point (i) 9th (tip) marker point

Figure 17: Displacements from marker points on the known steady state to marker points on the computed steady state in a system of $N = 8$ patches. Note that the displacements are not radial.

We see that, except for the rear and tip points, each marker point gets translated toward the tip under the parabolic ars model. In other words, there is a slight arclength expansion near the rear of the surface and a slight contraction near the tip. Some investigation has shown that this effect is coming from the integration of term (3) in Equation 1 but it is unclear exactly why. The likely answer has to do with the quantity $\sin(\alpha(s))/r(s)$, which is exactly the circumferential curvature κ_θ. When the surface is a sphere, κ_θ is constant, but the computed parabolic arcs are unable to produce constant κ_θ. From a cursory exploration on spheres it seems that the parabolic patches have accurate κ_θ at their midpoints but this accuracy deteriorates as we consider points on the patch closer to the endpoints.

6 Error analysis

Each model exhibits three types of error:

- Strain error: error arising from approximating the strains and propagating through computation;
- Integration error: error arising from the integration technique;
- Path error: error arising from the choice of interpolating curve on each patch.

Of these, the path error is the hardest to quantify because for a fixed set of marker points, one can give an arbitrarily wild curve passing through those marker points. With this in mind, we aim to quantify the other two types of error.

6.1 Error quantification in the abstract sense

For the strain error, the key observation is that we approximate the reciprocal of meridional strain $\frac{ds_0}{ds}$ by $\frac{l_0}{l}$, i.e. the quotient of the patch's intrinsic length by its deformed length. For the i-th patch, we have

$$s_0^{i+1} - s_0^i = \int_{s_i}^{s_{i+1}} \frac{ds_0}{ds}\, ds = \frac{ds_0}{ds}(c)(s_{i+1} - s_i) \implies \frac{ds_0}{ds}(c) = \frac{s_0^{i+1} - s_0^i}{s_{i+1} - s_i} = \frac{l_0^{i+1/2}}{l^{i+1/2}}$$

for some $c \in [s_i, s_{i+1}]$ by the mean value theorem for integrals. But then for any $\xi \in [s_i, s_{i+1}]$,

$$\frac{ds_0}{ds}(\xi) = \frac{ds_0}{ds}(c) + \int_c^\xi \frac{d^2 s_0}{ds^2}\, ds.$$

Therefore, if M is an upper bound on $\left|\frac{d^2 s_0}{ds^2}\right|$ over $[s_i, s_{i+1}]$, then the error is bounded above by $Ml^{i+1/2}$. In other words, there is error $O(l^{i+1/2})$ in the meridional strain and $O(l^{i+1/2}) + O(l_0^{i+1/2})$ in the tensions. This error decreases to 0 with finer discretization.

For the integration error, we use a similar argument. Suppose we want to approximate $\int_a^b f(x)\, dx$. Again by the MVT, there exists some $c \in [a, b]$ such that

$$\int_a^b f(x)\, dx = f(c)(b - a).$$

But then for any $\xi \in [a, b]$, we have

$$\int_a^b f(x)\, dx = \left(f(\xi) + \int_\xi^c f(x)\, dx\right)(b - a) = f(\xi)(b - a) + \left(\int_\xi^c f(x)\, dx\right)(b - a),$$

which is to say that we can approximate $\int_a^b f(x)\, dx$ by $f(\xi)(b - a)$ with error of

$$\left|\left(\int_\xi^c f(x)\, dx\right)(b - a)\right| \le \left(\int_a^b |f(x)|\, dx\right)(b - a) \le \left(\int_a^b M\, dx\right)(b - a) = M(b - a)(b - a) = M(b - a)^2,$$

where M is an upper bound for $|f'(x)|$ over the interval $[a, b]$. In other words, using endpoint rule to numerically evaluate the integral will yield error of $O(M(b - a)^2)$.

6.2 Error analysis in the linear and degenerate parabolic models

In our error analysis, we will quantify the error associated with integrating each force term over the right-hand half-patch $[s_i, s^{i+1/2}]$ of the i-th marker point. The error on the left half-patch is similar. For the term associated with $\frac{d(\sigma_s \hat{t})}{ds}$, it suffices to look at the error in $\sigma_s \hat{t}$ at $s = s^{i+1/2}$.

For the error in the linear model, we consider the stress error and the integration error associated with a numerical Riemann-Stieltjes integral with respect to $d\ln(r(s))$. Thus the force terms S_1, S_2, S_3, S_4 have the

following errors $E_{L1}, E_{L2}, E_{L3}, E_{L4}$:

$$S_1 : \sigma_s \hat{t} = \hat{t}\left(\frac{\mu}{2}\left(\frac{r_0^2}{r^2} - \frac{l_0^2}{l^2}\right) + K\left(\frac{r}{r_0}\frac{l}{l_0} - 1\right) + O(l) + O(l_0)\right) \implies E_{L1} = O(l + l_0), \tag{29}$$

$$\begin{aligned} S_2 : \int_{s_i}^{s^{i+1/2}} \frac{\sigma_s - \sigma_\theta}{r}\hat{r}\, ds &= \int_{s_i}^{s^{i+1/2}} \left(\mu\left(\frac{r_0^2}{r^2} - \frac{l_0^2}{l^2}\right) + O(l) + O(l_0)\right)\frac{\hat{r}}{r}\, ds \\ &= \hat{r}\int_{s_i}^{s^{i+1/2}} \left(\mu\left(\frac{r_0^2}{r^2} - \frac{l_0^2}{l^2}\right) + O(l) + O(l_0)\right)\, d\ln(r(s)) \\ &= \hat{r}\left[\mu\left(\frac{r_0^2}{r^2} - \frac{l_0^2}{l^2}\right)\right]_{s^{i+1/2}} \ln\left(\frac{r^{i+1/2}}{r_i}\right) + O\left(\ln\left(\frac{r^{i+1/2}}{r_i}\right)^2 (1 + l + l_0)\right) \\ &\implies E_{L2} = O\left(\ln\left(\frac{r^{i+1/2}}{r_i}\right)^2\right), \end{aligned} \tag{30}$$

$$\begin{aligned} S_3 : \int_{s_i}^{s^{i+1/2}} \frac{\sigma_s \sin\alpha}{r}\hat{n}\, ds &= \hat{n}\sin\alpha \int_{s_i}^{s^{i+1/2}} \frac{1}{r}\left(\frac{\mu}{2}\left(\frac{r_0^2}{r^2} - \frac{l_0^2}{l^2}\right) + K\left(\frac{r}{r_0}\frac{l}{l_0} - 1\right) + O(l) + O(l_0)\right)\, ds \\ &= \hat{n}\sin\alpha \int_{s_i}^{s^{i+1/2}} \frac{\mu}{2}\left(\frac{r_0^2}{r^2} - \frac{l_0^2}{l^2}\right) + K\left(\frac{r}{r_0}\frac{l}{l_0} - 1\right) + O(l) + O(l_0)\, d\ln(r(s)) \\ &= \hat{n}\sin\alpha\left[\frac{\mu}{2}\left(\frac{r_0^2}{r^2} - \frac{l_0^2}{l^2}\right) + K\left(\frac{r}{r_0}\frac{l}{l_0} - 1\right)\right]_{s^{i+1/2}} \ln\left(\frac{r^{i+1/2}}{r_i}\right) + O\left(\ln\left(\frac{r^{i+1/2}}{r_i}\right)^2 (1 + l + l_0)\right) \\ &\implies E_{L3} = O\left(\ln\left(\frac{r^{i+1/2}}{r_i}\right)^2\right), \end{aligned} \tag{31}$$

$$S_4 : \text{no stress error or integration error} \implies E_{L4} = 0. \tag{32}$$

In the computation for S_2, we applied the fact that the derivative of the integrand is

$$\frac{d(r_0^2/r^2)}{d(\ln(r))} \overset{y=\ln(r)}{=} \frac{d(r_0(e^y)^2/(e^y)^2)}{dy} = 2r_0'(e^y)\frac{r_0(e^y)}{e^y} - 2\frac{r_0(e^y)^2}{(e^y)^2} = 2r_0'\frac{r_0}{r} - 2\frac{r_0^2}{r^2}$$

which is bounded in absolute value as $r_0, r \to 0$ by some constant c provided that we assume the strain $r/r_0 \approx 1$. For S_3 we omit a similar computation showing $d(r_0/r)/d\ln(r)$ is bounded. In presenting the final estimates E_2 and E_3 we have discarded the factor $1+l+l_0$ because for a fine enough discretization this quantity is always bounded. Overall this shows that the error in the linear segments model is $O\left(\ln\left(\frac{r^{i+1/2}}{r_i}\right)^2\right)$.

For the degenerate parabolic model, the analysis is similar, except naive endpoint rule with respect to ds is used instead of a numerical Riemann-Stieltjes integral with respect to $d\ln(r(s))$. In this model the force

terms S_1, S_2, S_3, S_4 have the following errors $E_{PD1}, E_{PD2}, E_{PD3}, E_{PD4}$:

$$S_1 : \sigma_s \hat{t} = \hat{t}\left(\frac{\mu}{2}\left(\frac{r_0^2}{r^2} - \frac{l_0^2}{l^2}\right) + K\left(\frac{r}{r_0}\frac{l}{l_0} - 1\right) + O(l) + O(l_0)\right) \implies E_{PD1} = O(l + l_0), \tag{33}$$

$$\begin{aligned} S_2 : \int_{s_i}^{s^{i+1/2}} \frac{\sigma_s - \sigma_\theta}{r}\hat{r}\, ds &= \int_{s_i}^{s^{i+1/2}} \left(\mu\left(\frac{r_0^2}{r^2} - \frac{l_0^2}{l^2}\right) + O(l) + O(l_0)\right)\frac{\hat{r}}{r}\, ds \\ &= \hat{r}\int_{s_i}^{s^{i+1/2}} \mu\frac{r_0^2}{r^3}\, ds + \hat{r}\int_{s_i}^{s^{i+1/2}} \frac{1}{r}\left(O(l) + O(l_0) - \mu\frac{l_0^2}{l^2}\right)\, ds \\ &= \hat{r}\left[\mu\frac{r_0^2}{r^3}\right]_{s^{i+1/2}} + O((r^{i+1/2})^{-2}(s^{i+1/2} - s_i)^2) + \hat{r}\left[\frac{1}{r}\left(O(l) + O(l_0) - \mu\frac{l_0^2}{l^2}\right)\right]_{s^{i+1/2}} \\ &\quad + O((l + l_0)(r^{i+1/2})^{-2}(s^{i+1/2} - s_i)^2) \implies E_{PD2} = O((r^{i+1/2})^{-2}(\Delta s)^2) \end{aligned} \tag{34}$$

$$\begin{aligned} S_3 : \int_{s_i}^{s^{i+1/2}} \frac{\sigma_s \sin\alpha}{r}\hat{n}\, ds &= \hat{n}\sin\alpha\int_{s_i}^{s^{i+1/2}} \frac{1}{r}\left(\frac{\mu}{2}\left(\frac{r_0^2}{r^2} - \frac{l_0^2}{l^2}\right) + K\left(\frac{r}{r_0}\frac{l}{l_0} - 1\right) + O(l) + O(l_0)\right)\, ds \\ &= \hat{n}\sin\alpha\int_{s_i}^{s^{i+1/2}} \frac{\mu}{2}\frac{r_0^2}{r^3}\, ds + \hat{n}\sin\alpha\int_{s_i}^{s^{i+1/2}} \frac{1}{r}\left(O(l) + O(l_0) - K - \frac{\mu}{2}\frac{l_0^2}{l^2}\right)\, ds + \hat{n}\sin\alpha\int_{s_i}^{s^{i+1/2}} \frac{K}{r_0}\, ds \\ &= \hat{n}\sin\alpha\left[\frac{\mu}{2}\frac{r_0^2}{r^3}\right]_{s^{i+1/2}} + O((r^{i+1/2})^{-2}(s^{i+1/2} - s_i)^2) + \hat{n}\sin\alpha\left[\frac{1}{r}\left(O(l) + O(l_0) - K - \frac{\mu}{2}\frac{l_0^2}{l^2}\right)\right]_{s^{i+1/2}} \\ &\quad + O((l + l_0)(r^{i+1/2})^{-2}(s^{i+1/2} - s_i)^2) + \hat{n}\sin\alpha\left[\frac{K}{r_0}\right]_{s^{i+1/2}} + O((r_0^{i+1/2})^{-2}(s^{i+1/2} - s_i)^2) \\ &\implies E_{PD3} = O((r^{i+1/2})^{-2}(\Delta s)^2) \end{aligned} \tag{35}$$

$$S_4 : \text{no stress error or integration error} \implies E_{PD4} = 0. \tag{36}$$

In the computations for S_2 and S_3, we used the fact that $d(1/r)/dr = r^{-2}$, $d(r_0^2/r^3)/dr = r^{-2}(2r_0' r_0/r - 3r_0^2/r^2)$, and $d(1/r_0)/dr = r_0' r_0^{-2}$, and noted that the second factor in $d(r_0^2/r^3)/dr$ is bounded when $r, r_0 \to 0$ assuming the strain $r/r_0 \approx 1$. This shows that the overall error in the degenerate parabolic model is $O((r^{i+1/2})^{-2}(\Delta s)^2)$.

To compare the error of these two models, we note that for a fixed discretization, Δs is bounded, so we can discard it to obtain the error estimation $O((r^{i+1/2})^{-2})$ in the degenerate parabolic case, and for the linear segments case, we can overestimate the error as $O(\ln(r^{i+1/2})^2)$. Even with this overestimate, the degenerate parabolic error still dominates in the sense that as $r^{i+1/2} \to 0$,

$$\frac{(r^{i+1/2})^{-2}}{\ln(r^{i+1/2})^2}$$

is unbounded. This means that the degenerate parabolic model should perform much worse than the linear segments model near the tip and this claim is supported by evidence from our simulations.

A similar analysis for the parabolic arcs model would be insightful but has not been completed.

7 Linear stability analysis

Up until now, we have failed to mention an important consideration of our models: stability. Our model, considered on a system of N patches, is essentially a $2N$-dimensional dynamical system on base manifold $M = \mathbb{R}^{2N}$ in which a point on the manifold M represents the coordinates of the $N + 1$ marker points in our model (dropping the two coordinates which are always fixed to be zero). Each model's force computation defines a flow on $\mathbb{R}^{2N}$ and we want to investigate the stability of these flows near the steady state. To do this, we compute the Jacobian of our force function at the steady state and examine its eigenvalues: if all eigenvalues have negative real part then the dynamical system is stable; if some eigenvalue has positive real part then the dynamical system is nonstable [Hun11].

The stability of this dynamical system near the steady state also has implications for the positional error. Denote by $F : \mathbb{R}^{2N} \to \mathbb{R}^{2N}$ the force function and $JF : \mathbb{R}^{2N} \to \mathbb{R}^{2N\times 2N}$ its Jacobian. Let $\vec{x} \in \mathbb{R}^{2N}$ be the equilibrium point of the force, i.e. $\vec{x}$ satisfies $F(\vec{x}) = \vec{0}$. Near $\vec{x}$ we can linearize F by

$$F(\vec{x} + \delta\vec{x}) = F(\vec{x}) + Jf(\vec{x})\delta\vec{x} = Jf(\vec{x})\delta\vec{x}, \tag{37}$$

where $\delta\vec{x}$ is a small perturbation in position. Denoting by $\delta\vec{b}$ the force residue at this point $\vec{x} + \delta\vec{x}$, we find that

$$\delta\vec{b} = Jf(\vec{x})\delta\vec{x} \implies \delta\vec{x} = (Jf(\vec{x}))^{-1}\delta\vec{b}. \tag{38}$$

Because a matrix and its inverse have reciprocal eigenvalues, this shows that the stability of the force to small perturbations in marker point position also means stability of marker point positions against small perturbations in force. However, if any eigenvalue of $Jf(\vec{x})$ has absolute value less than 1, then $(Jf(\vec{x}))^{-1}$ may magnify error coming from the force residue, causing more positional error.

7.1 Exact stability analysis for small N

Even for small discretized systems, computing the Jacobian of the force function is a very complicated process. We worked out one example. For the linear segments model applied to a system of $N = 2$ patches initially in spherical configuration, we were able to compute the Jacobian of the force function using computer algebra, finding that the largest eigenvalue was approximately -0.66. This indicates stability. The corresponding work for the parabolic arcs and degenerate parabolic arcs models is left for the future.

7.2 Numerical stability analysis on spheres and ellipses for the ODE solver

For systems with many patches or nonspherical initial configuration, the stability analysis becomes unfeasible to by hand or computer algebra. Instead, we performed a numerical version of the stability analysis using the following procedure:

1. Fix half-widths a, b of an ellipse. Set up the initial membrane configuration so that the marker points are on this ellipse.
2. Run the simulation in each of the three models (linear, parabolic, and degenerate parabolic), and save the coordinates of the marker points in the computed steady state.
3. Numerically compute the Jacobian matrix for the force function under each of the three models at the corresponding steady states, and discard the first and last row and column (as these correspond to fixed coordinates).
4. Compute the eigenvalues of each Jacobian and check if they all have negative real part.

We used $N = 16$ patches, and the numerical Jacobian computation was performed using the DERIVESTsuite by John D'Errico [D'E20]. We performed this process for $a, b \in \{1, 2, 4\}$ and in each case we found that the maximum eigenvalue real part λ_1 for all three models (linear, parabolic, and degenerate parabolic) were approximately equal. These approximate eigenvalues, valid for all three of our models, are given in Figure 18.

λ_1	$a = 1$	$a = 2$	$a = 4$
$b = 1$	-0.19	-0.13	-0.08
$b = 2$	-0.15	-0.13	-0.11
$b = 4$	-0.11	-0.11	-0.11

Figure 18: The maximum real parts of the eigenvalues of the Jacobian in the steady state for initial ellipses of half-widths a and b in the $\hat{z}$ and $\hat{r}$-directions, respectively. These eigenvalues are approximately accurate for all three models (linear, parabolic, and degenerate parabolic).

In each case, the eigenvalues all have negative real parts. This suggests that in general each of the three models will be stable, at least for $N = 16$ patches and presumably larger N. Furthermore, we observe a rough inverse correlation between $|\lambda_1|$ and $\frac{a}{b}$, which together with Equation 38 may partially explain the dependence of the parabolic model's success on the initial marker point configuration.

8 Conclusion and future work

We have presented three discretized models for simulating the deformation of surfaces of revolution. While the basic linear segments model is rather standard and is comparatively easy to set up, the parabolic arcs model is more intricate. The degenerate parabolic arcs model serves little purpose in real usage, but does act as a benchmark to which the other two models can be compared.

Although the parabolic arcs model shows improved order of accuracy compared to the linear segments model, we have observed that the magnitude of this improvement is dependent on the intrinsic shape of the surface. Despite some weak correlation between order of accuracy and eigenvalues of the Jacobian in the steady state, the precise details of the relationship between convergence and initial geometry are not yet clear and should be pursued in the future. The parabolic arcs model is also more robust to external force, which may be useful in applications. As part of understanding the details of the parabolic arcs model's successes and drawbacks, we plan to analyze its error as described in Section 6. Because this model is significantly more complicated than the other two, this analysis will be more difficult. Furthermore, the error analysis will not tell the whole story, because it only takes into account the strain and integration errors, not the path error, which is where the parabolic arcs model shines. As we observed in the comparison between the linear and degenerate parabolic models in Section 6.2, naive numerical integration introduces significant error, so the fact that the parabolic arcs model still manages to improve on the linear segments model shows that the parabolic arcs must significantly reduce the path error.

On the topic of path error, we mentioned in Section 6 that the path error can likely be arbitrarily large. Despite this, we may be able to bound the path error subject to some geometric constraint on the true generating curve. This would reveal the full details of the error associated with each model.

Also yet to be understood is the convergence properties of each model with respect to curvature. In the future we should investigate the behavior in this respect. With this in hand, we can consider the sensitivity of each interpolation method to small perturbations in marker point positions. The sensitivity of the linear segments model to such perturbations has been analyzed before in [Che+20], and we plan to do the same for the parabolic and degenerate parabolic models. Stability analysis for these two models should also be done in order to obtain a full picture of the dynamics of each.

Our models are currently able to simulate the deformation of surfaces without any growth or atrophy. In this state, the models could already be used for some applications; for example, in simulating cell nucleus force sensing one can reasonably expect that little material change will take place on short timescales. However, in order to model morphogenesis of walled cells, growth will need to be incorporated. Luckily the highly compartmentalized design of our simulation software will make this implementation smooth.

Although the models we have presented are rather general in terms of their modeling assumptions, we always have kept in mind the analogy to membranes on the cellular level. Mathematical modeling on this scale is a rich area with many exciting developments and tremendous power to improve our understanding of the biological world. We hope that the work we present here represents a useful contribution to this field.

References

[Poz92] Constantine Pozrikidis. *Boundary integral and singularity methods for linearized viscous flow*. 1st ed. Cambridge, UK: Cambridge University Press, 1992.

[GT03a] Alain Goriely and Michael Tabor. "Biomechanical models of hyphal growth in actinomycetes". In: *Journal of Theoretical Biology* 222.2 (2003), pp. 211 –218. ISSN: 0022-5193. DOI: https://doi.org/10.1016/S0022-5193(03)00029-8. URL: http://www.sciencedirect.com/science/article/pii/S0022519303000298.

[GT03b] Alain Goriely and Michael Tabor. "Self-Similar Tip Growth in Filamentary Organisms". In: *Phys. Rev. Lett.* 90 (10 2003), p. 108101. DOI: 10.1103/PhysRevLett.90.108101. URL: https://link.aps.org/doi/10.1103/PhysRevLett.90.108101.

[GTT09] A. Goriely, M. Tabor, and A. Tongen. "A Morpho-Elastic Model of Hyphal Tip Growth in Filamentous Organisms". In: *IUTAM Symposium on Cellular, Molecular and Tissue Mechanics*. Springer Netherlands, Oct. 2009, pp. 245–255. DOI: 10.1007/978-90-481-3348-2_21. URL: https://doi.org/10.1007/978-90-481-3348-2_21.

[Hun11] John K. Hunter. *Introduction to Dynamical Systems*. Lecture notes. 2011.

[Dim12] P. Dimitrakopoulos. "Analysis of the variation in the determination of the shear modulus of the erythrocyte membrane: Effects of the constitutive law and membrane modeling". In: *Phys. Rev. E* 85 (4 2012), p. 041917. DOI: 10.1103/PhysRevE.85.041917. URL: https://link.aps.org/doi/10.1103/PhysRevE.85.041917.

[WBA15] Min Wu and Martine Ben Amar. "Modelling fibers in growing disks of soft tissues". In: *Mathematics and Mechanics of Solids* 20.6 (2015), pp. 663–679.

[Yan+15] Makoto Yanagisawa et al. "Patterning mechanisms of cytoskeletal and cell wall systems during leaf trichome morphogenesis". eng. In: *Nature plants* 1.3 (2015), pp. 15014–. ISSN: 2055-0278.

[EA+17] Alberto Elosegui-Artola et al. "Force Triggers YAP Nuclear Entry by Regulating Transport across Nuclear Pores". In: *Cell* 171.6 (2017), 1397 –1410.e14. ISSN: 0092-8674. DOI: https://doi.org/10.1016/j.cell.2017.10.008. URL: http://www.sciencedirect.com/science/article/pii/S0092867417311923.

[Xu+18] Muzhi Xu et al. "A scheme for 3-dimensional morphological reconstruction and force inference in the early C. elegans embryo". In: *PLOS ONE* 13.7 (July 2018), pp. 1–20. DOI: 10.1371/journal.pone.0199151. URL: https://doi.org/10.1371/journal.pone.0199151.

[Che+20] Danush Chelladurai et al. "Inferring lateral tension distribution in wall structures of single cells". eng. In: *European physical journal plus* 135.8 (2020). ISSN: 2190-5444.

[D'E20] John D'Errico. *Adaptive Robust Numerical Differentiation*. https://www.mathworks.com/matlabcentral/fileexchange/13490-adaptive-robust-numerical-differentiation. Retrieved November 14, 2020. 2020.